

SCIENTIFIC REPORTS



OPEN

Greener Route for Synthesis of aryl and alkyl-14H-dibenzo [a,j] xanthenes using Graphene Oxide-Copper Ferrite Nanocomposite as a Recyclable Heterogeneous Catalyst

Aniket Kumar¹, Lipeeka Rout¹, Lakkoji Satish Kumar Achary¹, Rajendra. S. Dhaka² & Priyabrat Dash¹

A facile, efficient and environmentally-friendly protocol for the synthesis of xanthenes by graphene oxide based nanocomposite (GO-CuFe₂O₄) has been developed by one-pot condensation route. The nanocomposite was designed by decorating copper ferrite nanoparticles on graphene oxide (GO) surface via a solution combustion route without the use of template. The as-synthesized GO-CuFe₂O₄ composite was comprehensively characterized by XRD, FTIR, Raman, SEM, EDX, HRTEM with EDS mapping, XPS, N₂ adsorption-desorption and ICP-OES techniques. This nanocomposite was then used in an operationally simple, cost effective, efficient and environmentally benign synthesis of 14H-dibenzo xanthene under solvent free condition. The present approach offers several advantages such as short reaction times, high yields, easy purification, a cleaner reaction, ease of recovery and reusability of the catalyst by a magnetic field. Based upon various controlled reaction results, a possible mechanism for xanthene synthesis over GO-CuFe₂O₄ catalyst was proposed. The superior catalytic activity of the GO-CuFe₂O₄ nanocomposite can be attributed to the synergistic interaction between GO and CuFe₂O₄ nanoparticles, high surface area and presence of small sized CuFe₂O₄ NPs. This versatile GO-CuFe₂O₄ nanocomposite synthesized via combustion method holds great promise for applications in wide range of industrially important catalytic reactions.

Xanthenes are important heterocycles with a variety of applications in the field of pharmaceutical chemistry¹. Notable pharmaceutical properties of xanthene derivatives are antibacterial², analgesic, antiviral³, anti-inflammatory⁴, antimalarial⁵ and anticancer⁶. These compounds have found wide use in dyes⁷, laser technologies and as pH-sensitive fluorescent materials⁸. Because of their usefulness, research on the catalytic preparation of xanthenes has attracted great attention. Mainly, condensation of aldehyde and 2-naphthol is the usual procedure for library synthesis of xanthenes, and its structural variants. A wide variety of catalysts have been reported in literatures for the synthesis of xanthenes such as *p*TSA⁹, sulfamic acid¹⁰, molecular iodine¹¹, tungsten heteropoly acid, silica sulphuric acid¹², NaHSO₄-SiO₂¹³, TiO₂-SO₄⁻²¹⁴, amberlyst-15¹⁵, wet cyanuric chloride¹⁶, K₅CoW₁₂O₄₀.3H₂O, acyclic acidic ionic liquids¹⁷, cellulose-sulphuric acid¹⁸, boric acid¹⁹ and Yb(OTf)₃²⁰. However, these catalysts suffer from one or more disadvantages, such as long reaction times, unsatisfactory yields, harsh reaction conditions, time taking work-ups, high cost, toxic solvent and difficulty in separation, justifying considerable scope for development of a noble catalyst for the synthesis of xanthenes via facile, energy efficient, easy separable and environmentally benign process.

Nanocatalysis, involving nanoparticles as catalyst has shown tremendous applications for a variety of organic transformations. Upto now, many investigations have been done on nanocatalysis, but there still remains the challenge of recovery of nanocatalyst from the reaction mixture. For this reason, magnetic nanoparticles have recently emerged as a useful group of nanocatalyst. The separation of magnetic nanoparticles is found to be simple and

¹Department of Chemistry, National Institute of Technology, Rourkela, Odisha, 769008, India. ²Novel Materials and Interface Physics Laboratory, Department of Physics, Indian Institute of Technology Delhi, Hauz Khas, New Delhi, 110016, India. Correspondence and requests for materials should be addressed to P.D. (email: dashp@nitrl.ac.in)

economical which diminishes the loss of catalyst, resulting in enhanced reusability. In addition, they exhibit high catalytic activity due to their large surface area and have relatively low preparation costs and toxicity. All these properties make them desirable and promising catalysts^{21–24} for industrial applications.

Among various magnetic nanoparticles, the copper ferrite, CuFe_2O_4 with a spinel structure, has been widely used in sensors, electronics and catalysis owing to its unique advantages such as environmental compatibility, moisture insensitive, high dispersion, high reactivity, low cost and easy separation by an external magnet. In catalysis, they are found to be a promising material for a variety of catalytic applications. For example, Amini *et al.* investigated the low temperature CO oxidation over mesoporous CuFe_2O_4 nanopowders synthesized by a novel sol–gel method²⁵. Parella *et al.* explored the catalytic application of CuFe_2O_4 nanoparticles for the Friedel–Crafts acylation²⁶. Feng *et al.* investigated the catalytic activity of CuFe_2O_4 nanoparticles for the reduction of 4-nitrophenol to 4-aminophenol with an excess amount of NaBH_4 ²⁷. To further improve the application efficiency of nanoparticles, various strategies have been employed over the years. One of the effective strategies is depositing nanoparticles on various carbon supports. These carbon hybrids are found to be highly active and selective catalyst as the result of the synergistic combination of both nanoparticle and carbon supports.

Graphene oxide, a two-dimensional sheet of sp^2 hybridized carbon has received increasing attention as it possesses similar properties to that of graphene. Because of its high surface area, mechanical and electrical properties and thermal stability it has been used as a significant supporting material and has been found as a promising material for fuel cells²⁸, sensors²⁹, solar cells³⁰, lithium batteries³¹ and organic synthesis³². In the catalysis front, owing to its large specific surface area, high chemical stability, good adsorption capacity, highly active and highly selective GO-based nanocatalysts have been designed by decorating GO surface with nanoparticles. The combination of the NPs and the graphene oxide sheets affords the composite better performance due to the synergistic interaction between the NPs and the graphene oxide sheets. These GO-based nanocatalyst mimic both homogeneous (high surface area and easily accessible) as well as heterogeneous (stable and easy to handle) catalyst systems³³. In addition to this, the presence of polar oxygen-containing functional groups, such as hydroxyl, epoxy, and carboxyl groups around GO prevents metal oxide nanoparticles from aggregation and leaching. Various metal oxides nanoparticles such as Fe_3O_4 ³⁴, CoFe_2O_4 ³⁵, ZnFe_2O_4 ³⁶, TiO_2 ³⁷, SnO_2 ³⁸ and ZnO ³⁹ were loaded on graphene oxide (GO) sheets, generating highly active and selective catalysts. Recently, our group designed graphene oxide– SnO_2 nanocomposite (GO– SnO_2) and used it as an efficient catalyst for the β -enaminones synthesis⁴⁰. Considering the benefits associated with both CuFe_2O_4 nanoparticles and GO, the combination of GO with CuFe_2O_4 would form a potential catalytic material and more recently, few studies have corroborated this fact^{27,41}. However, to our best knowledge, there has been no report yet on the use of graphene oxide–copper ferrite (GO– CuFe_2O_4) magnetic nanocomposite as a catalyst for biologically important xanthenes derivatives syntheses.

The methods to synthesize GO-based nanocomposites are diverse, such as hydrothermal²⁷, solvothermal⁴², and co-precipitation method⁴³. However above mentioned methods had some disadvantages such as time consuming, expensive, pollution causing and low yields. One method which has attracted a great deal of research in generating various metal oxide nanostructures is solution combustion synthesis (SCS). SCS is a time and energy-saving method as compared with other routes, especially for the preparation of complex oxides which can be easily adapted for scale-up applications⁴⁴. This method is economical both in terms of energy consumption and time. It is a simple, safe and rapid fabrication process for easily affordable porous materials due to their inherent characteristics. Many oxide nanostructures such as TiO_2 ⁴⁵, ZnO ⁴⁶, SnO_2 ⁴⁷, BiVO_4 ^{48,49}, ZrO_2 ⁵⁰, Co_3O_4 ^{51–53} and WO_3 ^{54,55} have been synthesised via SCS route. Various nanocomposites including ZnO - Fe_2O_3 ⁵⁶, TiO_2 - SiO_2 , TiO_2 - ZrO_2 , and TiO_2 - Al_2O_3 were also prepared by this method⁵⁷. Therefore, we envisioned that this quick, straightforward process can be used to synthesize highly porous GO– CuFe_2O_4 nanocomposite that can enhance the catalytic activity of a reaction by providing more adsorption and reaction sites during the reaction.

Herein, we report the successful synthesis of highly porous GO– CuFe_2O_4 nanocomposite through a solution combustion route and subsequently, for the first time the use of this material as a promising heterogeneous catalyst for xanthenes synthesis have been demonstrated. The xanthenes synthesis was obtained via two-component coupling of aromatic aldehyde and 2-naphthol in the presence of GO– CuFe_2O_4 nanocatalyst and the same protocol was applied to other xanthenes derivatives syntheses. All the reactions proceeded in a shorter period of time compared to traditional catalysts. Moreover, the catalyst can be recycled and reused up to five cycles with minimal loss in activity in a solvent free system. Our methodology may provide insight into the design of nanocatalysts using combustion route for its use in many more industrially important catalytic applications.

Results and Discussion

Structure and morphology characterization. Compared to the techniques employed for the preparation of nanocomposites such as solvothermal, hydrothermal and wet impregnation method, SCS is both energy and time efficient. Moreover, it can easily afford porous materials during the combustion process which is advantageous for adsorption of organic reactants on the nanocatalyst⁵⁸. During the synthesis, hydrated nitrates as metal salts are used as metal precursors due to the efficient oxidizing power of NO_3^- groups and its lower decomposition temperature and good solubility in water⁵⁹. Urea ($\text{CO}(\text{NH}_2)_2$) was used as a common fuel due to its low cost, good availability, high exothermicity, as well as their high coordination ability toward nitrates which help in controlling the size of nanoparticles⁵⁹. The samples obtained after the SCS synthesis was then characterized by various characterization techniques as outlined below.

FTIR spectra were recorded to study the effective incorporation of CuFe_2O_4 nanoparticles on GO matrix and presence of different functional groups present in the nanocomposite material. Figure 1(i) displays FTIR spectra of the the GO– CuFe_2O_4 nanocomposite. As shown in Fig. 1(i), the broad absorption band at $3400\text{--}3500\text{ cm}^{-1}$ in the FT-IR spectra of GO sample is associated with the stretching vibration of the $-\text{OH}$ group. The peak at 1728 cm^{-1} corresponds to the stretching of the $-\text{C}=\text{O}$ and $-\text{COOH}$ groups on GO sheets. The peak at 1616 cm^{-1} (aromatic $\text{C}=\text{C}$) can be ascribed to the skeletal vibrations of un-oxidized graphene domains. The $\text{C}-\text{O}$ bond is

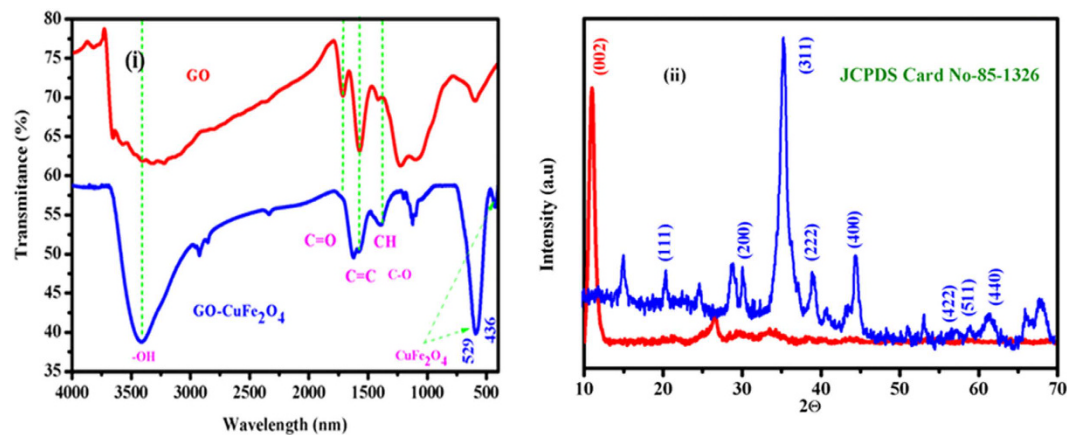


Figure 1. (i) FTIR spectra of GO and GO-CuFe₂O₄ nanocomposite and (ii) XRD powdered spectra of GO and GO-CuFe₂O₄ nanocomposite.

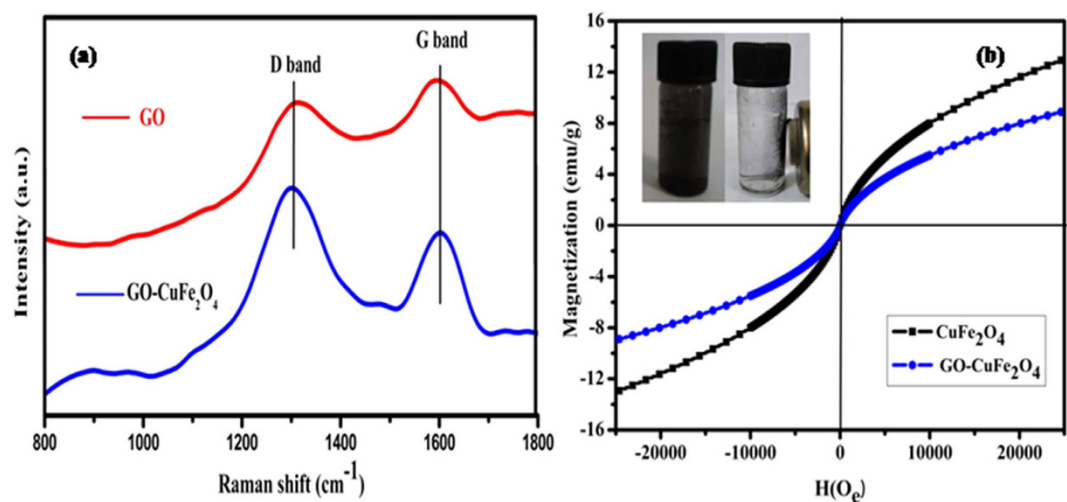


Figure 2. (a) Raman spectra of GO and GO-CuFe₂O₄ nanocomposite, and (b) Hysteresis loops of pure CuFe₂O₄ and GO-CuFe₂O₄. The inset is the magnetic separation property of GO-CuFe₂O₄ nanocomposite.

associated with the band at 1047 cm⁻¹. These observations are in good agreement with previous literatures^{60,61}. In the FTIR spectrum of GO-CuFe₂O₄, the presence of two absorption bands at 562 cm⁻¹ and 480 cm⁻¹ can be noticed. The absorption band at around 529 cm⁻¹ belongs to the stretching vibration of Cu²⁺ in octahedral site and the absorption band at around 436 cm⁻¹ belongs to the stretching vibration of Fe³⁺ in the tetrahedral site of CuFe₂O₄ nanoparticles, respectively⁶². It is interesting to find that after the composite synthesis, the peaks at 1047 cm⁻¹ are still present in the spectrum which suggests the minor reduction of functional groups after the composite synthesis.

XRD is a powerful technique to analyze the phase purity and crystal structure of the material. Figure 1(ii) displays the XRD spectrum of GO and GO-CuFe₂O₄ composites, wherein all the peaks can be assigned to cubic CuFe₂O₄ spinel structure. It is interesting to find that no impurity peaks of copper oxides (Cu₂O or CuO) were observed in the spectrum^{27,41,63,64}. A series of characteristic diffraction peaks observed at 30.5, 35.2, 57.0, 62.8 and 74.1 correspond to (220), (311), (511), (440) and (533) crystal planes of CuFe₂O₄, respectively (JCPDS card no: 85-1326). Moreover, no typical diffraction peak of GO (001) or RGO (002) was observed in the XRD spectrum suggesting that the GO in the GO-CuFe₂O₄ composite was fully exfoliated due to the crystal growth of CuFe₂O₄ nanoparticles between the interlayer of GO sheets, which results in the low diffraction intensity of GO⁴¹. The presence of broad peaks suggests the formation of smaller nanoparticles and particle size was found to be around 10 nm calculated using Debye-Scherrer formula⁶⁵⁻⁶⁷. All the above results demonstrate that during the composite synthesis GO sheets help in the controlled synthesis and the stabilization of the NPs.

To further confirm the effective reduction of GO during the composite synthesis and possible electronic interaction between GO and CuFe₂O₄ NPs, Raman measurements were carried out and are shown in Fig. 2(a). Similar to GO, GO-CuFe₂O₄ has two prominent D and G bands at 1354 and 1606 cm⁻¹, respectively. A small shifting of the bands in comparison to that of GO suggest the increase in disorderness on the GO surface. It is well known

Samples	Magnetic properties		
	M_s (emu g^{-1})	H_C (Oe)	M_R (emu g^{-1})
$CuFe_2O_4$	13.0	824	16.21
GO- $CuFe_2O_4$	8.1	1246	8.46

Table 1. Magnetic properties of $CuFe_2O_4$ and GO- $CuFe_2O_4$ nanocomposite.

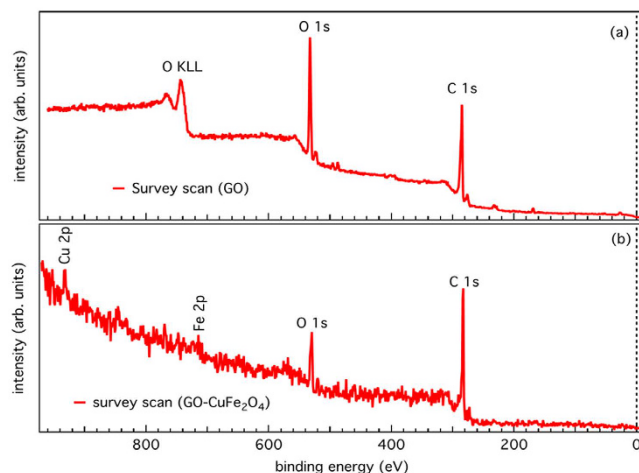


Figure 3. XPS survey scan of (a) GO and (b) GO- $CuFe_2O_4$ nanocomposite samples.

that the D band arises due to the defects in the graphene sheets whereas the G band arises due to the E_{2g} mode arising due to the sp^2 hybridised carbon domains⁶⁸. The D/G band intensity ratio ($I_D/I_G = 0.97$) of GO- $CuFe_2O_4$ was found to be larger than that of GO ($I_D/I_G = 0.86$). This suggests the possible electronic interaction between the GO and $CuFe_2O_4$ NPs which results in the reestablishment of conjugated graphene oxide network (sp^2) after loading of $CuFe_2O_4$ nanoparticles⁶⁹.

In order to check the magnetic properties of the as-obtained pure $CuFe_2O_4$ and GO- $CuFe_2O_4$ nanocomposite, magnetic measurement was carried out by VSM technique at room temperature and the results are shown in Fig. 2(b). The magnetic hysteresis loops of $CuFe_2O_4$ and GO- $CuFe_2O_4$ are an S-like curve that confirms the strong magnetic response to a varying magnetic field. The specific saturation magnetization (M_s) was found to be 13.0 emu/g for $CuFe_2O_4$ and 8.1 emu/g for GO- $CuFe_2O_4$ composite revealing the superparamagnetic behavior of both the samples. It should be pointed out that the saturation magnetization (M_s) values decreased after the loading of GO. The values of coercivity and remanence are summarized in Table 1. When an external magnetic field was applied for 20 s, rapid aggregation of the catalysts can be observed from their homogeneous dispersion (as shown in the inset of Fig. 2b). This observation suggests that the GO- $CuFe_2O_4$ nanocatalyst can be easily separated from the solution phase using an external magnet, which is important in practical applications.

A non-monochromatic Mg K α ($h\nu = 1253.6$ eV) X-ray source and PHOIBOS 150 electron energy analyzer from SPECS GmbH, Germany was used to acquiring X-ray photoelectron spectroscopy (XPS) measurements with the base pressure below 1×10^{-9} mbar. We have investigated the chemical composition and electronic structure of the GO- $CuFe_2O_4$ nanocomposite. The presence of the core-level peaks in XPS survey spectra, as shown in Fig. 3(a,b), indicates the existence of Fe, Cu, O, and C elements in $CuFe_2O_4$ and GO samples. In Fig. 4(a,b), we show the C 1s XPS spectrum of GO and GO- $CuFe_2O_4$ nanocomposite samples. For GO, the main peak positioned at around 284.5 eV, is assigned to non-oxygenated ring carbon molecules, while alternate peaks at 286.7, 287.8 and 289.1 eV are assigned to the oxygen-containing groups (C–OH), (C=O), and (O=C–OH), respectively (Fig. 4a). The C 1s core-level spectrum of GO- $CuFe_2O_4$ sample demonstrates that there is no significant change in intensity of the oxygenated functionalities in comparison to that of GO (Fig. 4b). This suggests the minor reduction of functional groups during the nanocomposite synthesis which is essential for the anchoring of metal nanoparticles on GO surface. In Fig. 4(c,d) we show the core-level spectra of Fe 2p and Cu 2p, respectively. The Fe 2p core-level spectrum shows two strong peaks at 710 and 722.8 eV, which are associated with Fe 2p_{3/2} and Fe 2p_{1/2} spin-orbit splitting, respectively. These are compared well with the Fe³⁺ octahedral species and the Fe³⁺ tetrahedral species^{70,71}. We also observed peaks at about 3 eV below the respective Fe 2p_{3/2} (Fe 2p_{1/2}) core-level peaks most probably due to FeO. Additionally, the satellite structure between the two peaks at 718 eV was the fingerprint of the electronic structure of Fe³⁺. Figure 4d shows the Cu 2p_{3/2} core level spectrum, which appears at 932.7 eV and is in accordance with Cu²⁺ states as reported in literatures⁷². A satellite peak is observed at 940.8 eV, which can be attributed to the formation of CuO. Overall, the XPS spectra of Cu 2p and Fe 2p show that Cu is in the +2 and Fe is in the +3 oxidation state in the nanocomposite, which is in good agreement with literatures on $CuFe_2O_4$ particles⁷³. These results indicate successful incorporation of $CuFe_2O_4$ nanoparticles (NPs) on graphene oxide sheets.

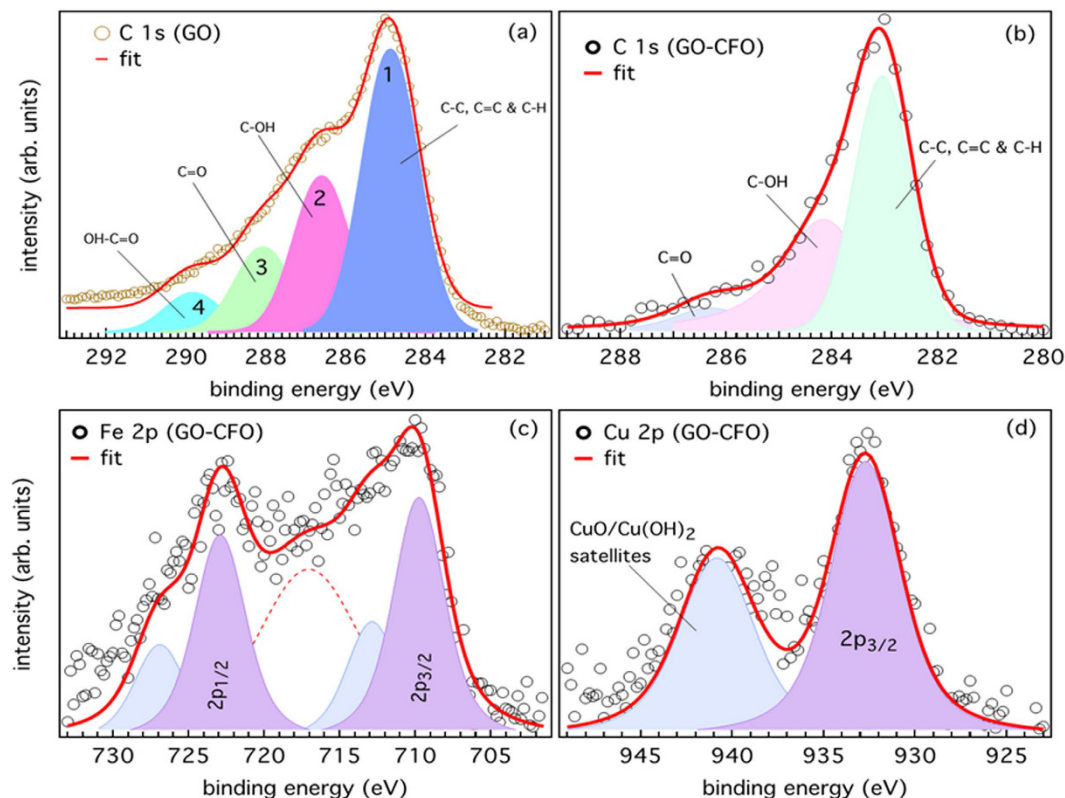


Figure 4. C 1s core-level spectra of (a) GO, (b) GO-CuFe₂O₄ nanocomposite samples. (c) Fe 2p and (d) Cu 2p core-levels of GO-CuFe₂O₄ sample.

The structural composition of GO and GO-CuFe₂O₄ was then ascertained by FESEM which are presented in Fig. 5. It is found from Fig. 5a that the GO exhibits thin sheet structure with wrinkled or folded morphology with a few stacked layers⁷⁴. Furthermore, the GO nanosheets appear as an isolated lamellar structure which is convenient for magnetic CuFe₂O₄ particle to anchor on its surface. Unlike graphene, GO sheets are expected to be “thicker” due to the presence of carbonyl, carboxyl, hydroxyl and epoxy groups above and below the original graphene planes. Figure 5b,c shows the morphology of GO-CuFe₂O₄ nanocomposite. The crumpled and layered structure of GO can be easily seen in the FESEM images (5b-c). Spherical CuFe₂O₄ nanoparticles of larger size ($\sim 121 \pm 2$ nm) are found to be homogeneously distributed on the GO surface indicating the agglomeration of synthesized nanoparticles.

Furthermore, the energy dispersive X-ray (EDX) analyses were recorded and are shown in the Fig. 5d. Elements such as C, O, Cu and Fe can be detected in the sample of GO-CuFe₂O₄. From EDX analysis it was confirmed that SCS could be an excellent and efficient route for the synthesis of graphene oxide based spinel nanocomposite. The EDX analysis showed that the distribution of the elements in the product was Cu = 14.28%, Fe = 28.95% and O = 56.77% (Table 2), thereby confirming the iron/copper ratio as 2.02 which is very much close to the atomic ratio in the formula CuFe₂O₄. Later on, to see the size, morphology, crystal structure, and elemental distribution in GO-CuFe₂O₄ composite, TEM and HRTEM with EDS mapping and scan were carried out. TEM images further demonstrate the layer structure of GO in the nanocomposite. From (Fig. 6a) TEM image, it can be seen that several individual CuFe₂O₄ particles seems to be agglomerated to form a bigger particle (size of 110 ± 2 nm) which sizes are found to be similar ($\sim 121 \pm 2$ nm) to that obtained from FESEM images. The size of the individual CuFe₂O₄ nanoparticles is of 10 ± 2 nm which can be clearly seen from Fig. 6b. This agglomeration and interconnection of individual CuFe₂O₄ nanoparticles can be attributed to the powerful inherent magnetic interaction of magnetic particles⁷⁵.

Moreover, the NPs were not observed outside the GO sheets indicating very good interactions between NPs and GO sheets. This homogeneous distribution of the CuFe₂O₄ NPs can possibly be one factor for the enhanced catalytic activity as described later. The crystalline nature of the composite was further confirmed by SAED analysis which depicts a ring-like structure (Fig. 6f). The (220), (311), (400), (511) and (440) rings are indexed to the tetragonal CuFe₂O₄. These patterns indicated that the nanoparticles are polycrystalline. HRTEM analysis (Fig. 6d) demonstrates the crystalline structure of GO-CuFe₂O₄ composite. The HRTEM image of the composite shown in Fig. 6d can be resolved into lattice fringe of 0.25 nm which can be indexed to (311) plane of spinel CuFe₂O₄. Later on, elemental mapping was carried to determine the elemental distribution of the individual components on the surface of CuFe₂O₄ nanoparticles, and the results are displayed in Fig. 7a. Energy-dispersive X-ray spectrometry (EDS) mapping analysis shows that the Cu, Fe and O elements are uniformly distributed in the CuFe₂O₄ nanoparticles, indicating the formation of spinel nanoparticles without phase segregation, as shown in Fig. 7 (red, Cu),

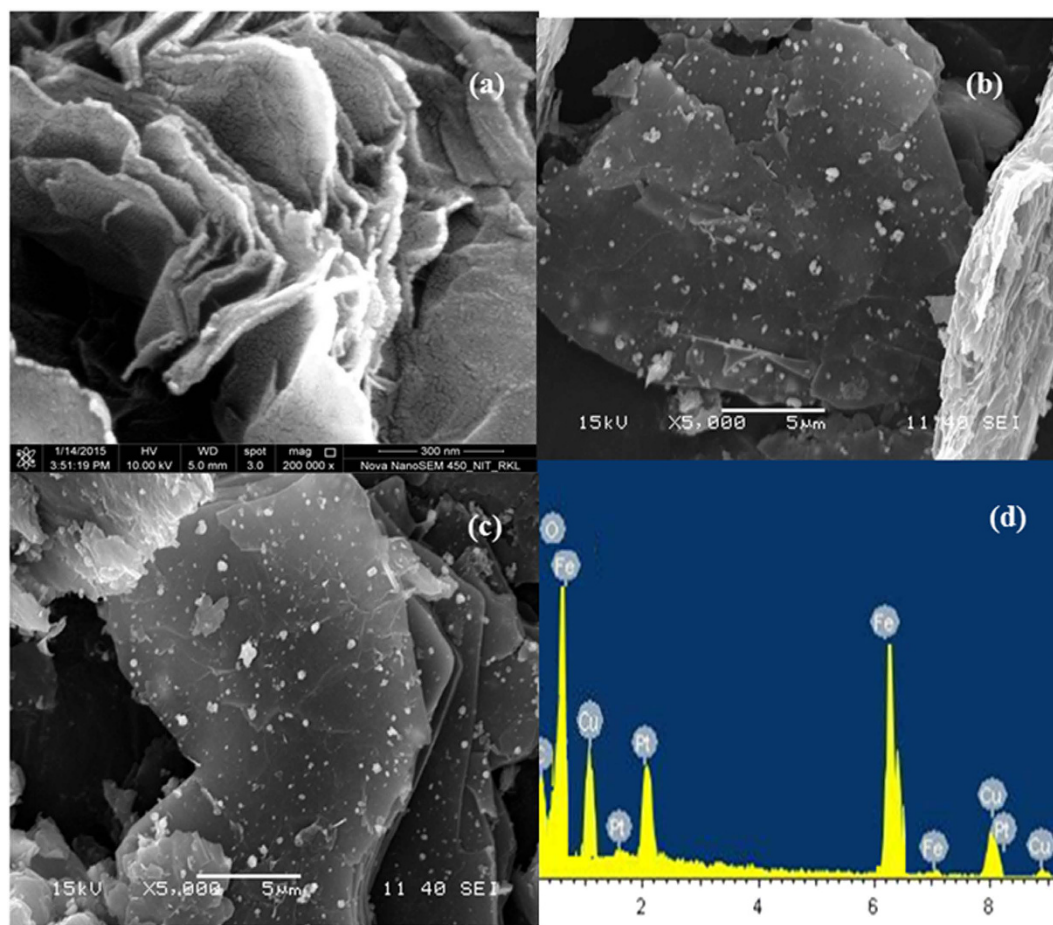


Figure 5. FE-SEM images of (a) GO and (b,c) GO-CuFe₂O₄ nanocomposite, (d) EDX of GO-CuFe₂O₄ nanocomposite.

Element	Weight %	Atomic %	Atomic ratio
O	56.77%	82.6	
Fe	28.95%	11.8	2.02
Cu	14.28%	5.6	1

Table 2. EDX compositions of GO-CuFe₂O₄ nanocomposite.

(green, Fe) and (blue, O). No traces of other impurities were seen in the spectra, suggesting that the synthesized composite are pure. The line scan along the direction derived in Fig. 7b demonstrated that all the elements are mixed well in the NPs. This further shows the high compositional uniformity of the GO-CuFe₂O₄ composite.

The surface area of the nanocomposite play an important role in the enhancement of catalytic activity by providing more adsorption and reaction sites during the reaction. To find the possible impact of SCS method on surface area and porosity, N₂ adsorption-desorption isotherm of CuFe₂O₄ and GO-CuFe₂O₄ composite were carried out and are shown in Fig. 8a. The BET surface area of CuFe₂O₄ and GO-CuFe₂O₄ nanocomposite exhibit type IV isotherm based on the IUPAC classification. The composite had a higher specific surface area (90 m²·g⁻¹) than that of CuFe₂O₄ (22 m²·g⁻¹). The surface area is found to be higher than other reported system synthesized by solvothermal method (35 m²·g⁻¹)⁶⁴. The average pore diameters in GO-CuFe₂O₄ composite were found to be 12 nm (Fig. 8b). This observed increase in the surface area could be one of the factors responsible for the enhanced catalytic activity of the GO-CuFe₂O₄ composite discussed later in detail.

TGA analysis is a useful analytical tool to study thermal stability of materials and to determine the composite composition. Therefore, TGA measurements of GO and GO-CuFe₂O₄ composites were measured in air atmosphere and are shown in Fig. 9. The GO has two weight losses of 41.4% and 59.2% at around 200 °C and 520 °C, respectively, which can be assigned to the degradation of GO and oxidation of carbon, respectively. In comparison, GO-CuFe₂O₄ shows a total mass loss of 33.2% when the temperature reaches 800 °C illustrating a much higher thermal stability than GO. According to the weight losses of GO-CuFe₂O₄, the amount of CuFe₂O₄ in the GO-CuFe₂O₄ is estimated to be about 33.5 wt %. Later on, the actual elemental composition and percentage

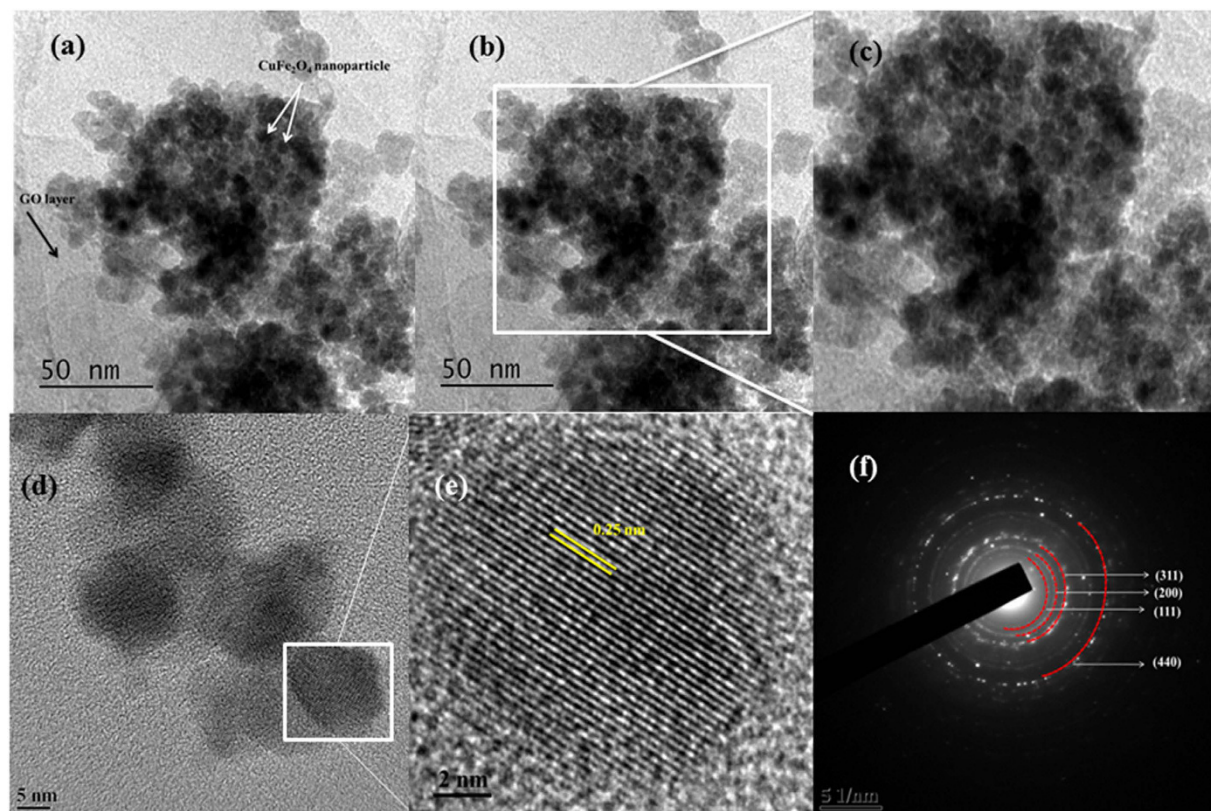


Figure 6. (a–e) TEM image of GO-CuFe₂O₄ nanocomposite at different magnification, (f) SAED image of GO-CuFe₂O₄ nanocomposite.

loading for GO-CuFe₂O₄ nanocomposite were further analysed by ICP-OES study. ICP analysis of 10 mg sample showed 1.96, 3.47 mg of Cu and Fe elements (i.e. 19.6% and 34.7%), respectively which means 7.43 mg of CuFe₂O₄ was loaded on graphene oxide sheets (i.e. 25.7% GO content). This 25.7% GO loading was in agreement with the TGA analysis as described above. ICP findings further confirmed that Cu and Fe are present in 1: 2 molar ratios which are consistent with stoichiometry of CuFe₂O₄ structure.

Catalytic Reactions. Till now many acid catalyst had been reported and it was found that they are showing an efficient path for synthesis of xanthenes and its derivative. But they suffer a lot of disadvantage notably due to their prolonged reaction time, tedious work condition, use of VOCs and hazardous reaction conditions. To overcome this problem the use of ILs as solvents as well as promoter in the synthesis have been reported, but high cost of imidazole, thiazole and pyridine based IL and use of costly catalyst for the synthesis have been the essential drawbacks. To overcome this drawback use of graphene oxide based nanocomposite can be promising catalytic material. Towards this objective the reaction of 2-naphthol (2 mmol) with benzaldehyde (1 mmol) was chosen as a model reaction at 125 °C under solventless condition to assess the catalytic performance of GO-CuFe₂O₄ nanocatalyst. The effects of various reaction parameters on reaction of 2-naphthol with benzaldehyde were also investigated. The products were characterized by FT-IR, ¹H-NMR and ¹³C-NMR spectroscopy.

To obtain the optimal reaction conditions, the effect of type of catalyst and catalyst dosage were initially investigated. Table 3 shows the yield of 14-phenyl-14H-dibenzo [a, j] xanthene (10a) in the presence and absence of catalyst. The reaction did not proceed in the absence of catalyst, but it increased in the presence of GO (20% yield) and CuFe₂O₄ nanoparticles (72% yield) (Table 3, entries 2 and 3). However, the combination of CuFe₂O₄ with appropriate amount of GO results in a dramatic enhancement of the catalytic activity of GO-CuFe₂O₄ (98% yield) (Table 3, entry 4). Since the support material takes an important role in catalysis, the impact of GO content on the catalytic activity of the GO-CuFe₂O₄ nanostructures was also investigated. The conversion rate of the reaction increased from 10 to 98% with increasing the loading amount of GO in GO-CuFe₂O₄ from 10–20% (Table 4, entries 1–5) and then decreased to 84% with further increase in loading.

This increase in catalytic activity of GO-CuFe₂O₄ composite can be attributed to the synergistic effect between the CuFe₂O₄ and the graphene oxide sheets. The presence of GO in the composite could enhance the adsorption of reactant molecules onto the catalytic sites of the GO-CuFe₂O₄ through π - π stacking and electrostatic interactions, leading to a high conversion rate. Additionally, the introduction of CuFe₂O₄ NPs into GO matrix results in its uniform dispersion on GO sheets and prevent them from agglomerating, thus increasing the number of active centers on CuFe₂O₄ nanoparticles. However, with further increase in GO amount beyond 20 wt% led to the lowering of active centres in the composite, which promoted less yield of the desired product. Therefore, 20 wt% was chosen as the required amount to carry out the reaction.

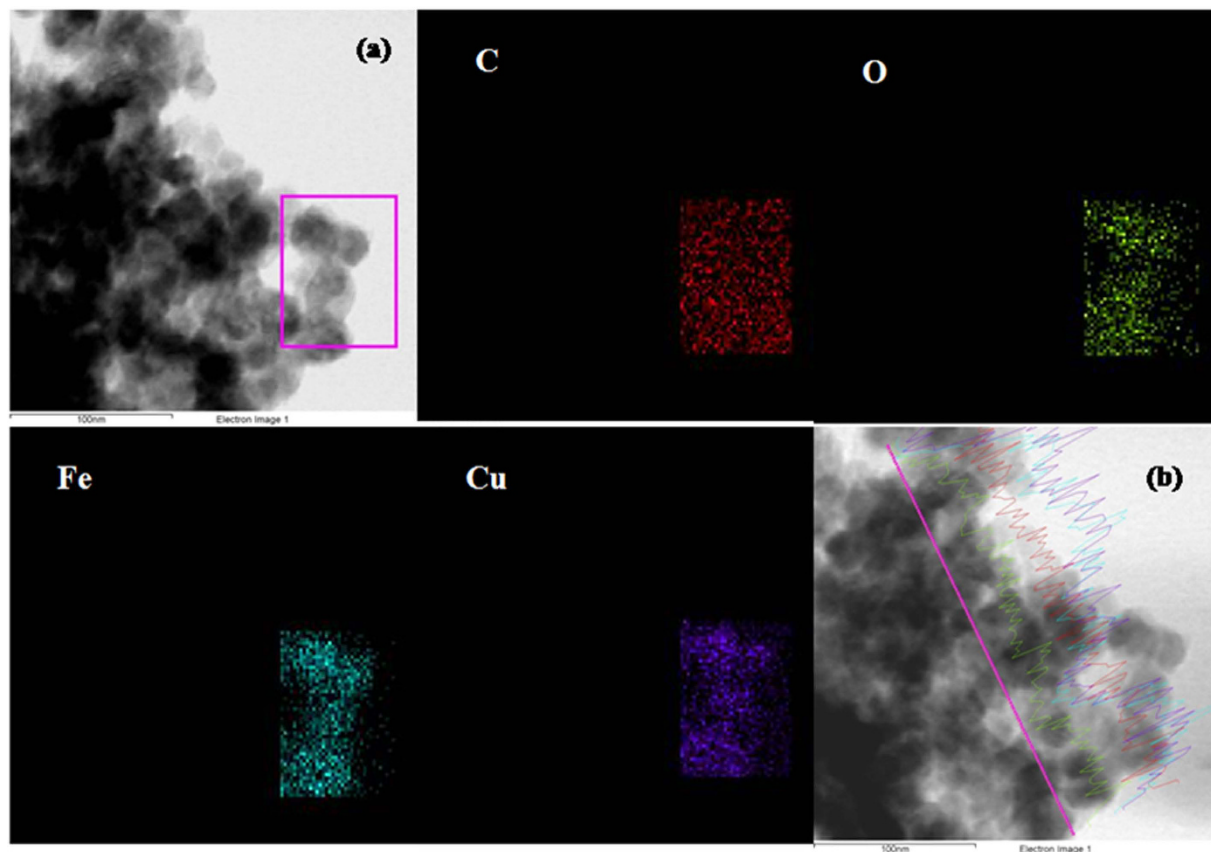


Figure 7. EDS mapping of (a) GO-CuFe₂O₄ nanocomposite and (b) EDS line scan of GO-CuFe₂O₄ nanocomposite.

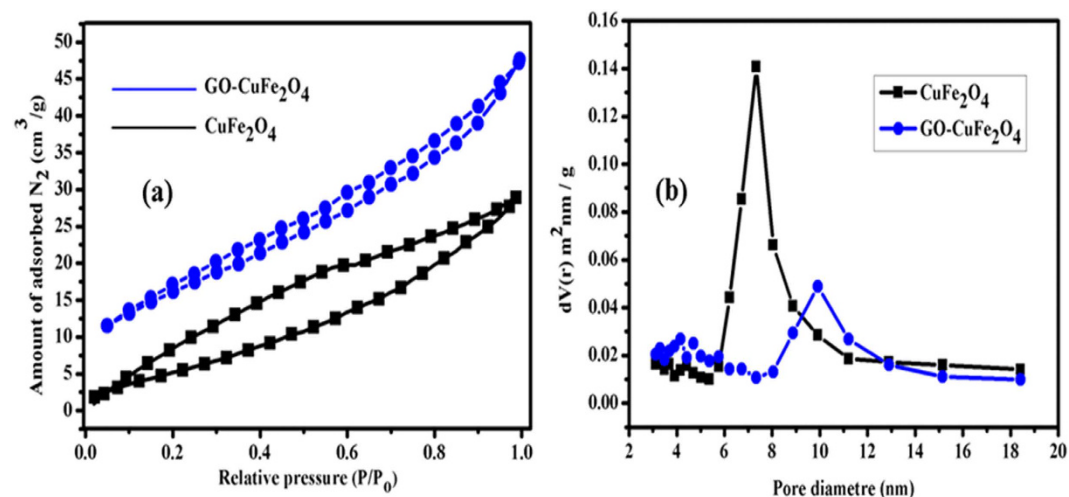


Figure 8. (a) Nitrogen adsorption/desorption isotherm and (b) pore size distribution of pure CuFe₂O₄ and GO-CuFe₂O₄ nanocomposite.

Later on, the effect of different dosages of GO-CuFe₂O₄ on xanthenes synthesis was examined (Table 5, Entry 1–7). The conversion rate increased from 60 to 98% with the rise of GO-CuFe₂O₄ doses from 5 to 20 mg. However, no significant difference was observed when the amount of catalyst was increased from 10 to 20 mg and yield lie above 90%. Theoretically, the amount of active sites on GO-CuFe₂O₄ rise with increasing dosage of catalyst, which increased the formation rate of xanthenes, and would promote the reaction to reach a higher conversion rate.

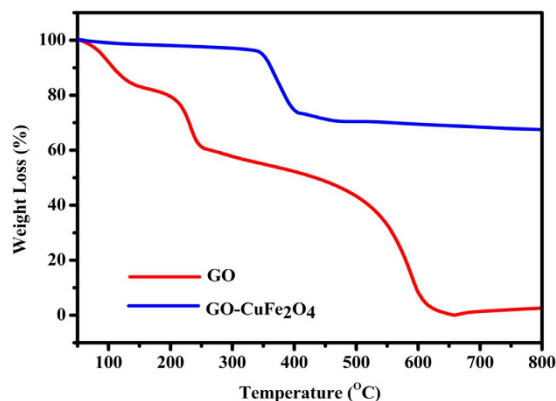


Figure 9. Thermogravimetric analysis (TGA) curves of GO, and GO-CuFe₂O₄ nanocomposite.

Entry	Catalyst	Yield (%) ^b
1.	Graphite	10
2.	GO	20
3.	CuFe ₂ O ₄ nanoparticle	72
4.	GO/CuFe ₂ O ₄	98
5.	CuO	52
6.	Fe ₃ O ₄	40
7.	Cu(NO ₃) ₂	12
8.	Fe(NO ₃) ₃	4
9.	Without catalyst	traces
10.	GO + CuFe ₂ O ₄ physical mixing	74
11.	CuFe ₂ O ₄ powder	52

Table 3. Effect of different catalysts on the reaction of 2-naphthol and benzaldehyde^a. ^aReaction conditions: 2-naphthol (2 mmol) and benzaldehyde (1 mmol). ^bIsolated yield.

Entry	Catalyst	Catalyst loading	Yield ^b (%)
1.	GO-CuFe ₂ O ₄	5 wt %	70
2.	GO-CuFe ₂ O ₄	10 wt %	82
3.	GO-CuFe ₂ O ₄	20 wt %	98
4.	GO-CuFe ₂ O ₄	30 wt %	92
5.	GO-CuFe ₂ O ₄	40 wt %	84

Table 4. Effect of different amount of catalysts loading, on the reaction of 2-naphthol and benzaldehyde^a. ^aReaction conditions: 2-naphthol (2 mmol) and benzaldehyde (1 mmol). ^bIsolated yield.

Entry	Amount of catalyst (mg)	Time (min)/% yield ^b
1.	Nil	60/nil
2.	5	30/60
3.	10	20/90
4.	15	15/92
5.	20	10/98

Table 5. Synthesis of 14H-dibenzo [a. j] xanthene using different amount of catalysts^a. ^aReaction conditions: 2-naphthol (2 mmol) and benzaldehyde (1 mmol). ^bIsolated yield.

Entry	Solvent	Catalyst	Catalyst loading	Temp (°C)	Yield ^b (%)
1.	H ₂ O	GO-CuFe ₂ O ₄	20 wt %	125	92
2.	Methanol	GO-CuFe ₂ O ₄	20 wt %	125	88
3.	Ethanol	GO-CuFe ₂ O ₄	20 wt %	125	84
4.	DCM	GO-CuFe ₂ O ₄	20 wt %	125	42
5.	Acetonitrile	GO-CuFe ₂ O ₄	20 wt %	125	50
6.	Toluene	GO-CuFe ₂ O ₄	20 wt %	125	60
7.	DMSO	GO-CuFe ₂ O ₄	20 wt %	125	68
8.	Hexane	GO-CuFe ₂ O ₄	20 wt %	125	20
9.	Solvent less	GO-CuFe ₂ O ₄	20 wt %	125	98

Table 6. Effect of solvent on the condensation of 14H-dibenzo [a, j] xanthene using GO-CuFe₂O₄ nanocatalyst^a. ^aReaction conditions: 2-naphthol (2 mmol) and benzaldehyde (1 mmol). ^bIsolated yield.

However, when the dosage of catalyst exceeded 20 mg, no obvious increase of the conversion rate was observed. Therefore, 20 mg of GO-CuFe₂O₄ was used in the subsequent experiments unless specifically stated (Table 5).

To check the efficiency of our catalyst, several other catalysts like graphite, GO, CuFe₂O₄, Fe₃O₄, CuO, Cu(NO₃)₂, and Fe(NO₃)₃ were also compared to GO-CuFe₂O₄ (Table-3, entries 1–9) and it was found that GO-CuFe₂O₄ is the best catalyst which requires shorter reaction times with higher yield (98%). Furthermore, our catalyst showed higher activity in comparison to other GO-CuFe₂O₄ system synthesized by other conventional methods like solvothermal and co-precipitation methods (Tables S2). All the above results demonstrate the usefulness of our catalyst for the synthesis of xanthenes. Type of solvents has pronounced effect on a catalytic reaction. In order to study this possible impact, the reaction of 2-naphthol (2 mmol) with benzaldehyde (1 mmol) was performed in different solvents and the summary of solvent effects are presented in Table 6. It can be found that the product yield is highest when the reaction was carried out in water (92% yields, (Table 6, entry 1). When we employed dichloromethane, acetonitrile, DMSO as the solvents, product 1a was generated in slightly low yields (Table 6, entries 4, 5, 7). Meanwhile, methanol, ethanol, n-hexane, toluene and water only afforded 1a in moderate or low yields (Table 6, entries 2, 3, 8).

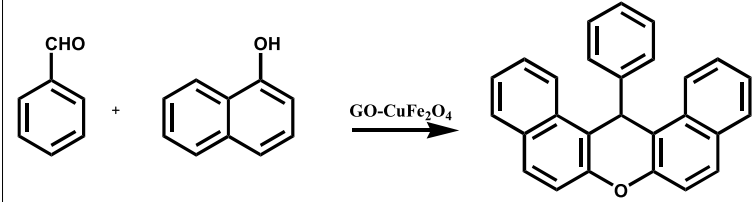
In addition, the reaction was carried out under solventless conditions and it was found that the reaction was carried out in very shorter reaction time and in higher yield under solventless condition (Table 6, entry 9). Therefore, solvent free conditions and using water as a solvent are obviously the best choices for these reactions. Catalytic reactions under solvent less condition are highly preferred as it reduces pollution and have low handling cost due to simplification of experimental method, workup techniques and time saving. Therefore, our method demonstrated a greener route for efficient synthesis of xanthene derivatives.

Then, we also briefly examined the effect of different temperatures, as reaction temperature has great impact on the catalysis of chemical reactions. The effect of temperatures was studied by carrying out the model reaction at different temperatures (r.t, 35, 75, 100, and 125 °C) in the presence of GO-CuFe₂O₄ catalyst under water and solvent less conditions (Table 7, entries 6–10). It was found that the conversion rate gradually increased with increasing of reaction temperature and the best result was obtained at 125 °C (Table 7, entries 5 and 10).

After optimizing the reaction conditions, we next investigated the generality of these conditions using 2-naphthol (2 mmol) and several aldehydes (1 mmol) both in H₂O and solvent less condition at 125 °C with 20 mg catalyst. The results are summarized in Fig. 10 (entries 10a to 10m). It can be seen that, our composite tolerated wide range of functional groups and all the reactions were completed within 10–18 min at 125 °C to give the desired products in excellent yields (82–98%) without forming any side products. It was exciting to know that the condensation products of xanthene formation were obtained in excellent yield under solvent less condition in lesser time with respect to the systems containing H₂O as solvent.

Later on, a wide range of aldehydes containing electron-withdrawing and electron donating groups were investigated. Aldehydes containing electron withdrawing groups such as chloro, bromo, and nitro underwent condensation in short reaction times with excellent isolated yields under both conditions (Fig. 10, entries 10h to 10m). Aldehyde containing electron-donating groups such as methyl, methoxy and hydroxyl required longer reaction time (Fig. 10, entries 10c to 10g). Therefore, the presence of electron-withdrawing and electron donating groups on the phenyl ring had affected the rate of reaction which indicates that there is clear electronic role of substituent. Also, for meta and para substituted groups, the rate of the reaction was affected which explain steric effect of substituents.

The presence of acidic site on catalyst surface plays an important role in the overall catalytic activity of chemical reaction. In general, xanthene syntheses are carried out conventionally with the use of Lewis and Brønsted acid catalysts^{9,10,76}. In our GO-CuFe₂O₄ catalyst, the acidic site in both GO and CuFe₂O₄ can therefore control the overall catalytic cycle. Numerous oxygen containing functionalities (e.g., alcohols and carboxylates) generated during the synthesis of GO via exhaustive oxidation provide Brønsted acidic sites to GO^{77–79}. At the same time, CuFe₂O₄ has strong Lewis acid character which originates primarily from the presence of tripositive Fe³⁺ and dipositive Cu²⁺ ions. The Lewis acidity of Fe³⁺ can be attributed due to its higher electronegativity while for Cu²⁺ this is due to acquirement of a stable and completely filled d-subshell on receiving an electron^{80–82}. As our GO-CuFe₂O₄ system has two acidic sites (GO as Bronsted site and CuFe₂O₄ as Lewis acid site) one would expect that Lewis and Brønsted acid site can play a synergistic role in the overall catalytic reaction.



Entry	Solvent	Catalyst	Catalyst loading	Temp (°C)	Yield ^b (%)
1.	Water	GO-CuFe ₂ O ₄	20 wt % GO/CuFe ₂ O ₄	r.t	8
2.	Water	GO-CuFe ₂ O ₄	20wt % GO/CuFe ₂ O ₄	35	30
3.	Water	GO-CuFe ₂ O ₄	20wt % GO/CuFe ₂ O ₄	70	58
4.	Water	GO-CuFe ₂ O ₄	20 wt % GO/CuFe ₂ O ₄	100	78
5.	Water	GO-CuFe ₂ O ₄	20 wt % GO/CuFe ₂ O ₄	125	92
6.	Solventless	GO-CuFe ₂ O ₄	20 wt % GO/CuFe ₂ O ₄	r.t	10
7.	Solventless	GO-CuFe ₂ O ₄	20 wt % GO/CuFe ₂ O ₄	35	40
8.	Solventless	GO-CuFe ₂ O ₄	20 wt % GO/CuFe ₂ O ₄	70	75
9.	Solventless	GO-CuFe ₂ O ₄	20 wt % GO/CuFe ₂ O ₄	100	88
10.	Solventless	GO-CuFe ₂ O ₄	20 wt % GO/CuFe ₂ O ₄	125	98

Table 7. Effect of temperature on the condensation of 14 H-dibenzo [a, j] xanthene using GO-CuFe₂O₄ nanocatalyst^a. ^aReaction conditions: 2-naphthol (2 mmol) and benzaldehyde (1 mmol). ^bIsolated yield.

In order to confirm the importance of synergistic interaction between GO and CuFe₂O₄, we compared the activity of GO-CuFe₂O₄ to that of a physical mixture of GO and CuFe₂O₄. It can be found that the catalytic activity of the reaction system containing physical mixture of GO and CuFe₂O₄ (74% yield) is similar to those observed for pure CuFe₂O₄ nanoparticles (72% yield), which is lower than that of GO-CuFe₂O₄ (98% yield) as shown in Table 3. These results indicated the possibility of synergism between GO and CuFe₂O₄ acidic sites in the xanthene synthesis. Similar synergistic effects in the final catalytic activity were reported in the literatures^{83–86}. Moreover, in GO-CuFe₂O₄ nanocomposite which was obtained by chemical method, the CuFe₂O₄ nanoparticles would exhibit strong interactions with graphene oxide sheets, thereby, strongly influencing the catalytic behaviour of the nanocomposite^{87,88}. On the other hand, a simple physical mixing cannot create effective interfacial contacts between the CuFe₂O₄ nanoparticles and graphene oxide sheets. As a result, slower diffusion and decrease of mass transfer of reactant molecules take place which would be the cause for the decrease in yield in case of physically mixed GO and CuFe₂O₄ NP system⁸⁹.

In addition, the crucial role of CuFe₂O₄ nanoparticles as good catalyst was also demonstrated. As can be seen from Table 3, CuFe₂O₄ nanoparticles which provide smaller particle size and higher surface area showed higher activity to that of powder CuFe₂O₄ samples^{86,90}. Moreover, in comparison to Fe₃O₄ samples, pure CuFe₂O₄ nanoparticles showed higher activity (table 3, entry 3), demonstrating the active role of Cu²⁺ in the catalytic reaction^{27,86,91}.

From all the results discussed above, a plausible mechanism for xanthene synthesis using GO-CuFe₂O₄ catalyst has been outlined in Fig. 11. The presence of strong acidic sites (both Lewis and Brønsted acid) in GO-CuFe₂O₄ nanocatalyst initially facilitates the efficient chemical adsorption of reactant molecules and favours the interaction of carbonyl group of aldehyde (IA) to the acidic sites^{78–80}. Because of this interaction, the carbonyl group of aldehyde was protonated/activated for nucleophilic attack in the subsequent steps and forms an intermediate form (IB). The Lewis acid site, Cu²⁺ and Fe³⁺ of CuFe₂O₄ nanoparticle that anchored onto the GO surface also co-ordinate with the intermediate by bonding with the –OH group, which further increases its electrophilic nature and helps in the stabilisation of intermediate^{92,93}. Finally, the intermediate (II) undergoes nucleophilic attack by a second molecule of β-naphthol to produce intermediate (III). The desired product is then formed by the cyclodehydration of intermediate (III) followed by dehydration. The coordination of CuFe₂O₄ NPs with the hydroxyl groups of intermediate help in increasing the electrophilicity of the intermediate and for subsequent nucleophilic attack of the β-naphthol molecule and in the cyclization process. It can be concluded that the Cu²⁺ and Fe³⁺ of CuFe₂O₄ nanoparticle help in activation and stabilization of substrate molecules during xanthenes synthesis.

Reproducibility of catalyst. Recovery of catalysts is important for the re-usage and application cost of a catalyst. Since GO-CuFe₂O₄ composite are found to be magnetic they can be easily removed from reaction solution with a magnet. Therefore, the catalytic stability of the GO-CuFe₂O₄ nanocomposite for the reaction of benzaldehyde (1 mmol) with naphthol (2 mmol) in the presence of 20 mg of GO-CuFe₂O₄ nanocomposite as catalyst was studied to give the desired product. After completion of the reaction (monitored by TLC), the catalyst was separated by applying an external magnetic field, washed with deionized water and acetone, and then vacuum dried at 60 °C for 3 h before being used in the subsequent recycling experiment. As shown in Fig. 12, GO-CuFe₂O₄ nanocomposite was still stable even after being recycled five times. The composite showed very high activity (yield 87 and 93%) even after 5th cycle without any accountable loss of activity. The recovered catalyst was

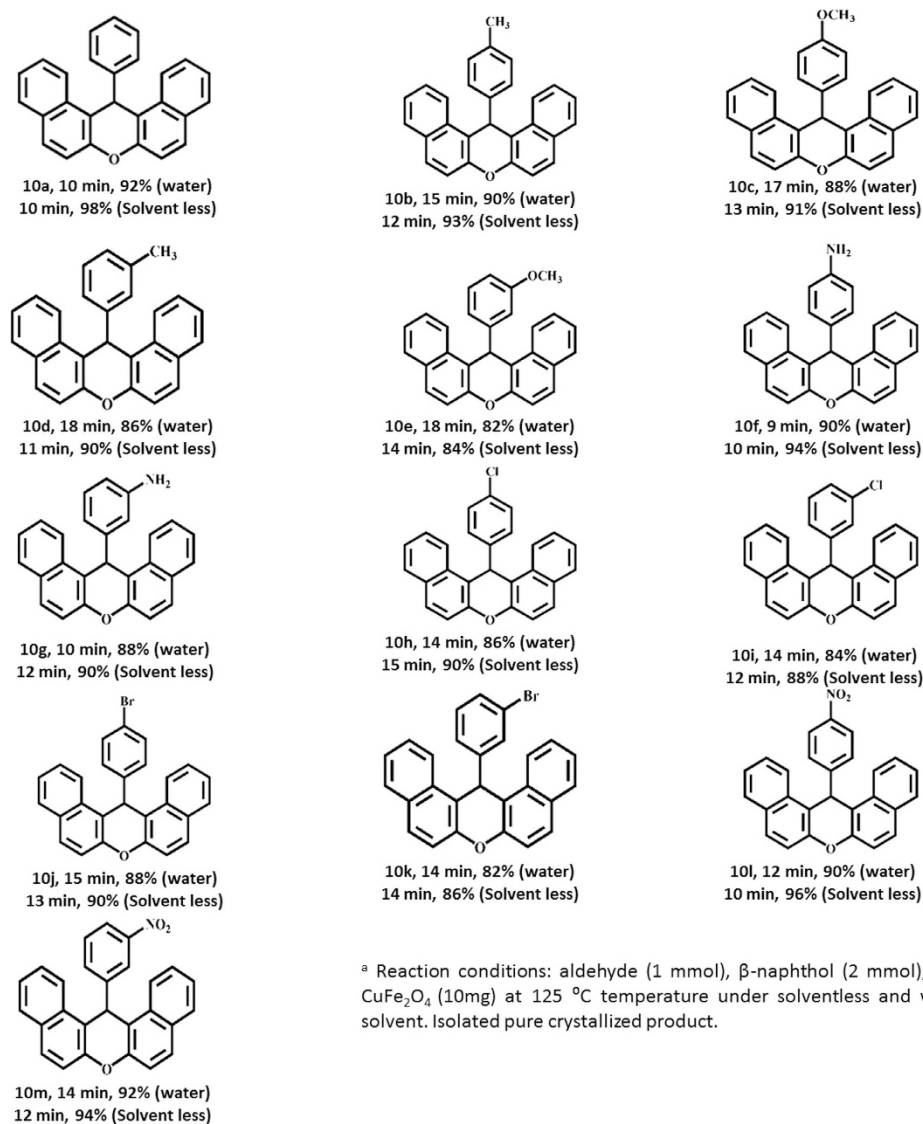


Figure 10. The one-pot synthesis of 14-aryl-14H-dibenzo-[a, j] xanthenes using GO-CuFe₂O₄ nanocomposite^a.

characterized by powder XRD which showed similar pattern with fresh sample indicating stability of spinel structure (see Fig. S1). Further, FESEM image (Fig. S1) showed similar morphology after 5th cycle. ICP analysis also showed very minute change in percentage loading (Cu: 1.91 and Fe: 3.34) as compared to original loading 1.96, 3.47 mg of Cu and Fe elements for copper ferrite NPs. This outstanding stability and recyclability of GO-CuFe₂O₄ nanocomposites can be ascribed to very good interaction between CuFe₂O₄ NPs and GO sheets which prevents agglomeration of the nanoparticles.

Comparison with other reported systems. Later on, to check the efficiency of our catalyst we have compared the activity of our catalyst with other reported catalysts. Table 8 shows the comparison of reported catalyst with our catalyst for the synthesis of xanthene under the same conditions. From Table 8, it can be seen that our catalyst exhibited higher yields in lesser time compared to the other reported system such as sulfamic acid¹⁰, [2-(sulfoxy)ethyl] sulfamic acid⁹⁴, Fe(HSO₄)₃⁹⁵, functionalized mesoporous materials⁹⁶, InCl₃/P₂O₅⁹⁷, HY zeolite⁹⁸ and K₅CoW₁₂O₄₀·3H₂O⁹⁹. These results confirmed that our GO-CuFe₂O₄ catalyst is more effective and less time consuming for synthesis of xanthenes under solventless condition.

Methods

Graphite powder and CDCl₃ were purchased from Sigma-Aldrich. Cu (NO₃)₂·3H₂O, Fe (NO₃)₃·9H₂O, H₂O₂ (30%), isopropanol, ethanol, NaNO₃, H₂SO₄ (98%), HCl, KMnO₄, urea and silica gel (100–200 mesh) were purchased from Hi-Media. All chemicals were used as received without further purification. 18 Milli-Ω water was used throughout the synthesis.

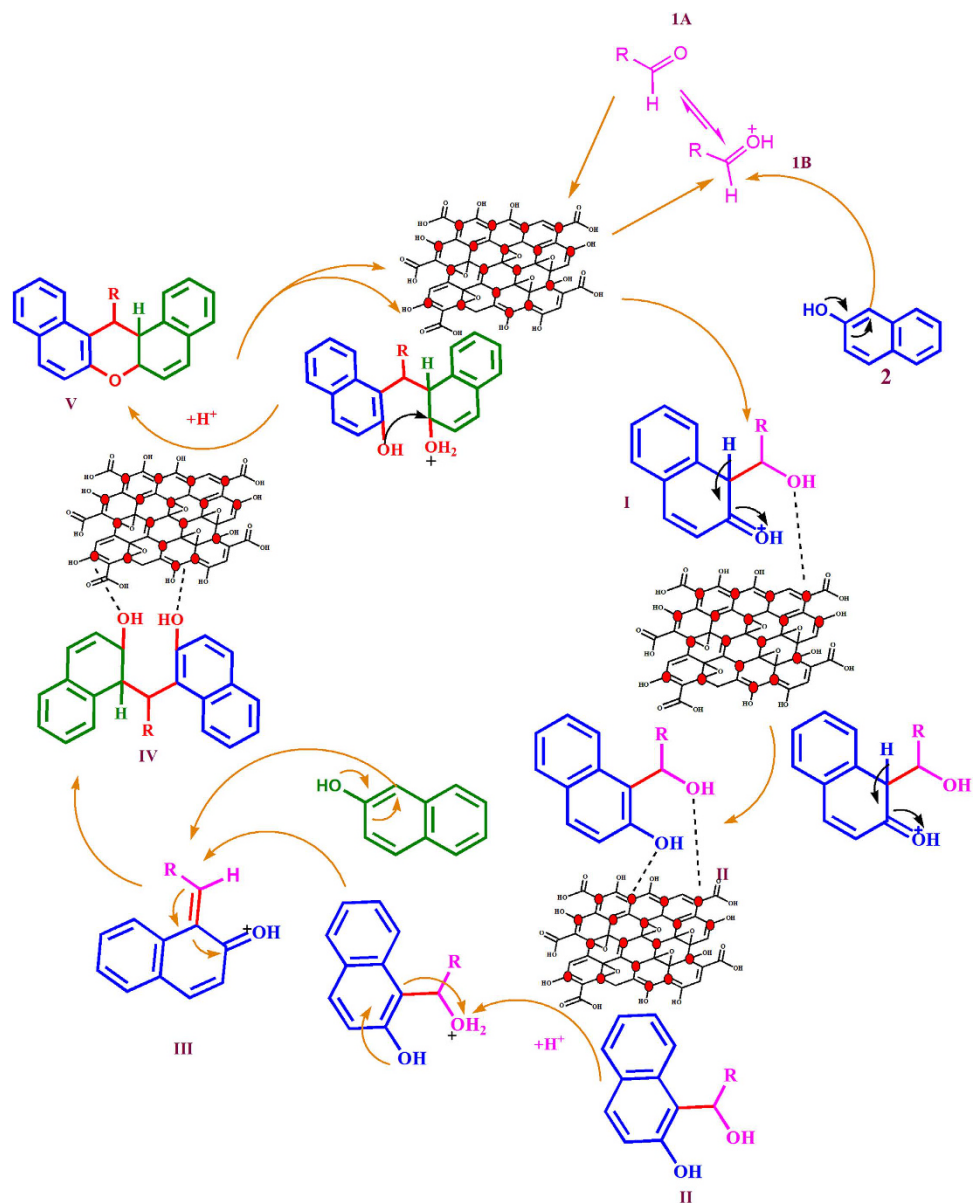


Figure 11. Plausible mechanism for the synthesis of xanthenes catalyzed by GO-CuFe₂O₄ nanocomposite.

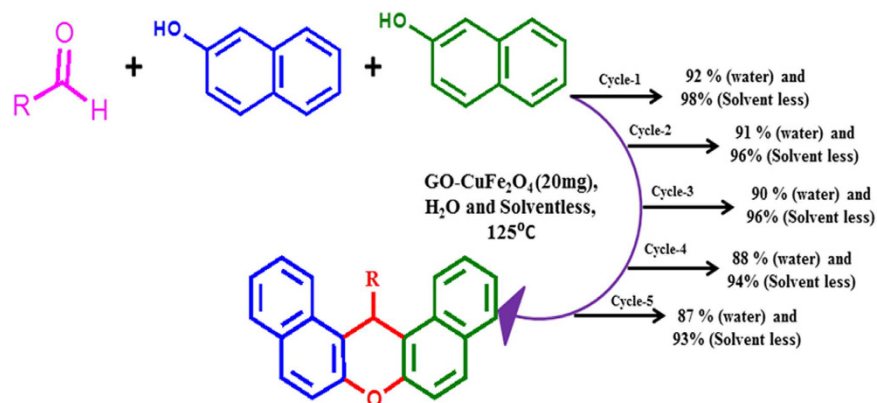


Figure 12. Recyclability study of the catalyst for the one-pot synthesis of 14-(phenyl) - 14H-dibenzo [a. j] xanthenes.

Entry	Catalyst	Amount of catalyst (mol %)	Temperature (°C)	Time (min)	Yield (%)	Solvent	Ref.
1.	Sulfamic acid	10	125	660	94	Solventless	10
2.	[2-(Sulfoxy)ethyl]sulfamic acid	15	150	20	76		94
3.	GO-CuFe ₂ O ₄	10	125	10	98	Solventless	Present Work
4.	GO-CuFe ₂ O ₄	10	125	15	92	H ₂ O	Present Work
5.	Fe(HSO ₄) ₃	35	—	420	85	DCM	95
6.	Functionalized mesoporous materials	20	25	360	80	DCM	96
7.	InCl ₃ /P ₂ O ₅	—	120	25–80	58–88		97
8.	HY zeolite	—	80	60–1440	80–94	Solventless	98
9.	K ₅ CoW ₁₂ O ₄₀ ·3H ₂ O	—	125	120	91	Solventless	99

Table 8. Comparison of the catalytic activity of GO-CuFe₂O₄ nanocomposite with the reported catalysts in the preparation of 14-(phenyl)-14H dibenzo [a. j] xanthenes.

Preparation of GO. GO was prepared from natural graphite powder through modified Hummers' method^{100–102}. In brief, 1 g of graphite was mixed to 25 ml to concentrated H₂SO₄ (98% w/w), followed by stirring at room temperature for 24 h. To the resulting pre-oxidized product, 100 mg of NaNO₃ was added to the mixture and stirred for 30 min. Subsequently, the mixture was kept below 5 °C using an ice bath and 3 g of KMnO₄ was slowly added to the mixture and the mixture was stirred for 2 h under the ice-water bath. After that about 250 ml distilled water and 20 ml H₂O₂ (30%) was added to dilute the solution at room temperature. After 10 min, a bright yellow solution was obtained and resulting solution was precipitated for 12 h, and the upper supernatant was collected and centrifuged. Successively, the GO powders were washed with 10% HCl and distilled water three times. The obtained GO was dispersed in distilled water to get a stable brown solution.

Preparation of the GO-CuFe₂O₄ nanocatalyst. The GO-CuFe₂O₄ nanocomposite materials were synthesized by a solution combustion synthesis. Initially solution A was formed by adding 0.242 g (0.001 mol) sample of Cu(NO₃)₂·3H₂O and 0.808 g (0.002 mol) of Fe(NO₃)₃·9H₂O to 20 mL of water and kept for stirring for 30 min at room temperature to form a homogeneous solution. Later on, solution B was prepared by dispersing 0.150 g of GO in deionized water (1.48 mL) and ethanol (18 mL), followed by 30 min ultrasonic treatment. Then, solution B was added dropwise to solution A under vigorous stirring. After 1 h stirring, urea was added as fuel to prepare the precursor solution. Finally, the precursor solution was heated on a hot plate at 100 °C to remove the solvent until a gel-like precursor was obtained. This precursor was introduced into a preheated muffle furnace at temperature of 400 °C in air and maintained for 10 min, during which combustion reaction took place. A black foam type GO-CuFe₂O₄ nanocomposite materials was obtained which was characterised by various analytical techniques and used as novel catalyst for xanthene synthesis (Fig. 13).

General procedure for the synthesis of xanthenes under solventless condition. A mixture of the aldehyde (1 mmol), β-naphthol (2 mmol), and GO-CuFe₂O₄ (10 mg) nanocomposite was stirred at 125 °C for 10–15 min. After the completion of the reaction as monitored by TLC, the reaction mixture was cooled to room temperature and solid obtained was dissolved in EtOAc (20 mL), followed by stirring the mixture for 10 min. Later on, this was filtered to separate the catalyst. The catalyst was washed with ethyl acetate (2 × 10 mL). The combined ethyl acetate extracts were washed with water (2 × 10 mL) and dried over Na₂SO₄. The crude product thus obtained was washed with hexane and cold ethanol. The purified product was then obtained after column chromatography. All products were characterized by comparison of their physical constants and spectral data with those for authentic samples.

General procedure for the synthesis of xanthenes in water media. A mixture of the aldehyde (1 mmol), β-naphthol (2 mmol), and GO-CuFe₂O₄ (10 mg) nanocomposite was stirred at 125 °C for 10–20 min in water as solvent. After the completion of the reaction as monitored by TLC, the reaction mixture was cooled to room temperature and solid obtained was dissolved in EtOAc (20 mL), followed by stirring the mixture for 10 min. Later on, this was filtered to separate the catalyst. The catalyst was washed with ethyl acetate (2 × 10 mL). The combined ethyl acetate extracts were washed with water (2 × 10 mL) and dried over Na₂SO₄. The crude product thus obtained was washed with hexane and cold ethanol. The purified product was then obtained after column chromatography. All products were characterized by comparison of their physical constants and spectral data with those for authentic samples.

Catalyst Characterizations. The catalyst was analysed by X-ray diffraction study using PHILIPS PW 1830 X-ray diffractometer with CuKα source. The compositional information of the products was performed using EDX (JEOL JSM-6480 LV). Raman spectra were recorded using a BRUKER RFS 27 spectrometer with 1064 nm wavelength incident laser light. Field emission scanning electron microscopy (FESEM) of the sample was recorded by Nova Nano SEM/FEI. Transmission electron micrographs (TEM) of the sample were recorded using PHILIPS CM 200 equipment using carbon coated copper grids. The contents of Cu and Fe in the catalyst were analysed using ICP-OES made by Perkin Elmer, USA, ALPHA ATB. Nitrogen adsorption/desorption isotherm was obtained at 77 K on a Quanta chrome Autosorb 3-B apparatus. The specific surface area and pore size

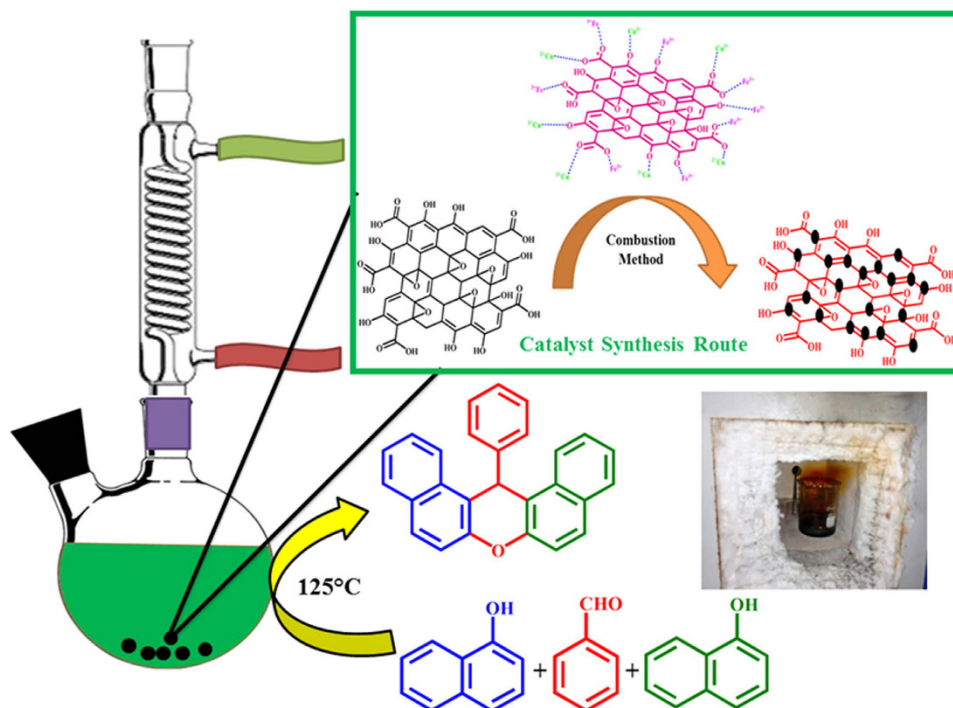


Figure 13. Preparation of GO-CuFe₂O₄ nanocomposite via SCS route for synthesis of xanthenes.

distribution were acquired by emulating BET equation and BJH method, respectively. ¹H NMR and ¹³C NMR spectra were recorded on a Bruker spectrometer at 400 MHz using TMS as an internal standard. FTIR spectra of the product were recorded using a Perkin-Elmer FTIR spectrophotometer using NaCl support. Magnetic properties of the sample were measured by vibrating sample magnetometer (Lakeshore VSM) at room temperature. A commercial electron energy analyzer (PHOIBOS 150 from Specs GmbH, Germany) and a non-monochromatic Mg K α x-ray source ($h\nu = 1253.6$ eV) have been used to perform XPS measurements with the base pressure of $<1 \times 10^{-9}$ mbar. Catalytic reactions were monitored by thin layer chromatography on 0.2 mm silica gel F-254 plates. All the reaction products are known compounds and have been identified by comparing their physical and spectral characteristics with the literature reported values.

Conclusions

In conclusion, an inexpensive and magnetically recyclable GO-CuFe₂O₄ nanocatalyst was synthesized by a simple combustion method. Using this nanocomposite, a facile, efficient and environmentally-friendly protocol for the synthesis of xanthenes was reported. The catalyst was thoroughly characterized by a set of analytical techniques. The formation of spinel nanoparticles was comprehensively demonstrated by EDS mapping and scan techniques. We have for the first time demonstrated the use of GO-CuFe₂O₄ as highly active and efficient nanocatalyst for the synthesis of xanthene derivatives via one-pot two-component reaction of 2-naphthol with various aryl aldehydes under solventless condition. The results demonstrated that the combination of CuFe₂O₄ with graphene oxide results in a dramatic enhancement of the catalytic activity of CuFe₂O₄, which can be attributed to the remarkable synergistic effect between the CuFe₂O₄ and the graphene oxide sheets. The promising points for the presented methodology are efficiency, generality, high yield, cleaner reaction profile and recyclability which make it a useful and attractive process for the synthesis of xanthenes as biologically interesting compounds.

References

1. Khurana, J. M. *et al.* Synthesis of novel 12-aryl-8,9,10,12-tetrahydrobenzo[a]xanthene-11-thiones and evaluation of their biocidal effects. *Eur. J. Med. Chem.* **58**, 470–477 (2012).
2. Hideo, T. & Teruomi, J. *Jpn. Patent Sankyo Co.* 5600–5480 (1981).
3. Hafez, H. N., Hegab, M. I., Ahmed-Farag, I. S. & ElGazzar, A. B. A. A facile regioselective synthesis of novel spiro-thioxanthene and spiro-xanthene-9',2'-[1,3,4]thiadiazole derivatives as potential analgesic and anti-inflammatory agents. *Bioorg. Med. Chem. Lett.* **18**, 4538–4543 (2008).
4. Jin, T. S., Liu, L. B., Zhao, Y. & Li, T.-S. Clean Synthesis of Compounds Containing Two 4H-Pyrons or Two Tetraketones in Aqueous Media. *Synth. Commun.* **35**, 2379–2385 (2005).
5. Chibale, K. *et al.* Exploring the potential of xanthene derivatives as trypanothione reductase inhibitors and chloroquine potentiating agents. *Tetrahedron Lett.* **59**, 2289–2296 (2003).
6. Shashidhara, K. V., Kumar, A., Dodda, R. P. & Kumar, B. A new iodine catalyzed regioselective synthesis of xanthene synthons. *Tetrahedron Lett.* **53**, 3281 (2012).
7. Zhang, W. & Xu, R. Hybrid photocatalytic H₂ evolution systems containing xanthene dyes and inorganic nickel based catalysts. *Int. J. Hydrogen Energy* **37**, 17899–17909 (2012).

8. Ojida, A., Takashima, I., Kohira, T., Nonaka, H. & Hamachi, I. Turn-on fluorescence sensing of nucleoside polyphosphates using a xanthene-based Zn(II) complex chemosensor. *J. Am. Chem. Soc.* **130**, 12095–12101 (2008).
9. Khosropour, A. R., Khodaei, M. M. & Moghannian, H. A facile, simple and convenient method for the synthesis of 14-alkyl or aryl-14-H-dibenzo[a,j]xanthenes catalyzed by p-TSA in solution and solvent-free conditions. *Synlett* **6**, 955–958 (2005).
10. Rajitha, B., Kumar, B. S., Reddy, Y. T., Reddy, P. N. & Sreenivasulu, N. Sulfamic acid: a novel and efficient catalyst for the synthesis of aryl-14H-dibenzo [a, j] xanthenes under conventional heating and microwave irradiation. *Tetrahedron Lett.* **46**, 8691–8693 (2005).
11. Pasha, M. A. & Jayashankara, V. P. Molecular iodine catalyzed synthesis of aryl-14H-dibenzo[a, j]xanthenes under solvent-free condition. *Bioorg. Med. Chem. Lett.* **17**, 621–623 (2007).
12. Kantevari, S., Bantu, R. & L. Nagarapu. HClO₄-SiO₂ and PPA-SiO₂ catalyzed efficient one-pot Knoevenagel condensation, Michael addition and cyclo-dehydration of dimedone and aldehydes in acetonitrile, aqueous and solvent free conditions: Scope and limitations. *J. Mol. Catal. A: Chem.* **269**, 53–57 (2007).
13. Das, B., Thirupathi, P., Reddy, K. R., Ravikanth, B. & Nagarapu, L. An efficient synthesis of 1,8-dioxo-octahydroxanthenes using heterogeneous catalysts. *Catal. Commun.* **7**, 535–538 (2007).
14. Jin, T. S., Zhang, J. S., Wang, A.-Q. & Li, T.-S. Solid-state condensation reactions between aldehydes and 5, 5-dimethyl-1, 3-cyclohexanedione by grinding at room temperature. *Synth. Commun.* **35**, 2339–2345 (2005).
15. Song, G., Wang, B., Luo, H. & Yang, L. Fe³⁺-montmorillonite as a cost-effective and recyclable solid acidic catalyst for the synthesis of xanthenediones. *Catal. Commun.* **8**, 673–676. (2007).
16. Zhang, Z.-H. & Tao, X.-Y. 2,4,6-Trichloro-1,3,5-Triazine-promoted synthesis of 1,8-Dioxo-Octahydroxanthenes under solvent-free conditions. *Aust. J. Chem.* **61**, 77–79 (2008).
17. Venkatesan, K., Pujari, S. S., Lahoti, R. J. & Srinivasan, K. V. An efficient synthesis of 1,8-dioxo-octahydro-xanthene derivatives promoted by a room temperature ionic liquid at ambient conditions under ultrasound irradiation. *Ultrason. Sonochem.* **15**, 548 (2008).
18. Oskooie, H. A., Tahershamsi, L., Heravi, M. M. & Baghernejad, B. Cellulose sulfonic acid: An efficient heterogeneous catalyst for the synthesis of 1, 8-Dioxo-octahydroxanthenes. *E- J. Chem.* **7**, 717–720 (2010).
19. Karimi-Jaberi, Z. & Keshavarzi, M. Efficient one-pot synthesis of 14-substituted-14H-dibenzo [a, j] xanthenes using boric acid under solvent-free conditions. *Chin. Chem. Lett.* **21**, 547–549 (2010).
20. Su, W., Yang, D., Jin, C. & Zhang, B. Yb(OTf)₃ catalyzed condensation reaction of β-naphthol and aldehyde in ionic liquids: a green synthesis of aryl-14H-dibenzo[a,j]xanthenes. *Tetrahedron Lett.* **49**, 3391–3394 (2008).
21. Mohammad, A. Z. *et al.* A highly stable and active magnetically separable Pd nanocatalyst in aqueous phase heterogeneously catalyzed couplings. *Green Chem.* **15**, 2132–2140 (2013).
22. Dandia, A., Jain, A. K. & Sharma, S. CuFe₂O₄ nanoparticles as a highly efficient and magnetically recoverable catalyst for the synthesis of medicinally privileged spiroprymidine scaffolds. *RSC Adv.* **3**, 2924–2934 (2013).
23. Reddy, K. H. V., Satish, G., Karnakar, K. R. K. & Nageswar, Y. V. D. Magnetically separable CuFe₂O₄ nanoparticle catalyzed C–Se cross coupling in reusable peg medium. *Chem. Lett.* **41**, 585–587 (2012).
24. Zhang, R. *et al.* Magnetic CuFe₂O₄ nanoparticles as an efficient catalyst for C–O cross-coupling of phenols with aryl halides. *ChemCatChem* **3**, 146–149 (2011).
25. Amini, E., Rezaei, M. & Sadeghinia, M. Low temperature CO oxidation over mesoporous CuFe₂O₄ nanopowders synthesized by a novel sol-gel method. *Chin. J. Catal.* **34**, 1762 (2013).
26. Parella, R., Kumar, A. N. & Babu, S. A. Catalytic Friedel–Crafts acylation: magnetic nanopowder CuFe₂O₄ as an efficient and magnetically separable catalyst. *Tetrahedron Lett.* **54**, 1738 (2013).
27. Zhang, H., Gao, S., Shang, N., Wang, C. & Wang, Z. Copper ferrite–graphene hybrid: a highly efficient magnetic catalyst for chemoselective reduction of nitroarenes. *RSC Adv.* **4**, 31328–31332 (2014).
28. kumar, G. G., Awan, Z., Nahm, K. S. & Xavier, J. S. Nanotubular MnO₂/graphene oxide composites for the application of open air-breathing cathode microbial fuel cells. *Biosens. Bioelectron.* **53**, 528–534 (2014).
29. Wang, X. *et al.* Highly dispersible and stable copper terephthalate metal–organic framework–graphene oxide nanocomposite for an electrochemical sensing application. *ACS Appl. Mater. Interfaces* **6**, 11573–11580 (2014).
30. Bajpai, R., Roy, S., Koratkar, N. & Misra, D. S. NiO nanoparticles deposited on graphene platelets as a cost-effective counter electrode in a dye sensitized solar cell. *Carbon* **56**, 56–63 (2013).
31. Dong, L. *et al.* Hydrothermal synthesis of mixed crystal phases TiO₂-reduced graphene oxide nanocomposites with small particle size for lithium ion batteries. *Int. J. Hydrogen Energy* **39**, 16116–16122 (2014).
32. Nie, R. *et al.* MnO₂/graphene oxide: a highly active catalyst for amide synthesis from alcohols and ammonia in aqueous media. *J. Mater. Chem.* **22**, 18115–18118 (2012).
33. Baig, R. B. N. & Varma, R. S. Magnetically retrievable catalysts for organic synthesis. *Chem. Comm.* **49**, 752–770 (2013).
34. He, G. *et al.* Fe₃O₄@graphene oxide composite: A magnetically separable and efficient catalyst for the reduction of nitroarenes. *Mater. Res. Bull.* **48**, 1885–1890 (2013).
35. Fu, Y., Chen, H., Sun, X. & Wang, X. Combination of cobalt ferrite and graphene: High-performance and recyclable visible-light photocatalysis. *Appl. Catal. B* **111–112**, 280–287 (2012).
36. Fu, Y. & Wang, X. Magnetically separable ZnFe₂O₄-graphene catalyst and its high photocatalytic performance under visible light irradiation. *Ind. Eng. Chem. Res.* **50**, 7210–7218 (2011).
37. Liang, Y., Wang, H., Casalogue, H. S., Chen, Z. & Dai, H. TiO₂ nanocrystals grown on graphene as advanced photocatalytic hybrid materials. *Nano Res.* **3**, 701–705 (2010).
38. Zhang, J., Xiong, Z. & Zhao, X. S. Graphene–metal–oxide composites for the degradation of dyes under visible light irradiation. *J. Mater. Chem.* **21**, 3634–3640 (2011).
39. Li, B. & Cao, H. ZnO@graphene composite with enhanced performance for the removal of dye from water. *J. Mater. Chem.* **21**, 3346 (2011).
40. Kumar, A., Rout, L., Dhaka, R. S., Samal, S. L. & Dash, P. Design of a graphene oxide-SnO₂ nanocomposite with superior catalytic efficiency for the synthesis of β-enaminones and β-enaminoesters. *RSC Adv.* **5**, 39193–39204 (2015).
41. Zhao, Y., He, G., Dai, W. & Chen, H. High catalytic activity in the phenol hydroxylation of magnetically separable CuFe₂O₄-reduced graphene oxide. *Ind. Eng. Chem. Res.* **53**, 12566–12574 (2014).
42. Zhang, W. *et al.* One-step facile solvothermal synthesis of copper ferrite–graphene composite as a high-performance supercapacitor material. *ACS Appl. Mater. Interfaces* **7**, 2404–2414 (2015).
43. Dhanda, R. & Kidwai, M. Magnetically separable CuFe₂O₄/reduced graphene oxide nanocomposites: as a highly active catalyst for solvent free oxidative coupling of amines to imines. *RSC Adv.* **6**, 53430–53437 (2016).
44. Li, F.-T., Ran, J., Jaroniec, M. & Qiao, S. Z. Solution combustion synthesis of metal oxide nanomaterials for energy storage and conversion. *Nanoscale* **7**, 17590–17610 (2015).
45. Chung, S. L. & Wang, C. M. Solution combustion synthesis of TiO and its use for fabrication of photo electro de for dye-sensitized solar cell. *J. Mat. Sci. Tec.* **28**, 713–722 (2012).
46. Ahmad, M. *et al.* Effect of fuel to oxidant molar ratio on the photocatalytic activity of ZnO nanopowders. *Ceram. Int.* **39**, 3007–3015 (2013).

47. Fraigi, L. B., Lamas, D. G. & Reca, N. E. W. d. Comparison between two combustion routes for the synthesis of nanocrystalline SnO₂ powders. *Mater. Lett.* **47**, 262–266 (2001).
48. Jiang, H. Q., Endo, H., Natori, H., Nagai, M. & Kobayashi, K. Microstructure, mechanical properties and stability of nitrided Y-TZP. *J. Eur. Ceram. Soc.* **28**, 2955–2962 (2008).
49. Zhang, Z., Wang, W., Shang, M. & Yin, W. Photocatalytic Degradation of Rhodamine B and Phenol by Solution Combustion Synthesized BiVO₄ Photocatalyst. *Catal. Comm.* **11**, 982–986 (2010).
50. Deshpande, P. A., Poliseti, S. & Madras, G. Rapid synthesis of ultrahigh adsorption capacity zirconia by a solution combustion technique. *Langmuir* **27**, 3578–3587 (2011).
51. Ai, L. H. & Jiang, J. Rapid synthesis of nanocrystalline Co₃O₄ by a microwave-assisted combustion method. *Powder Technol.* **195**, 11 (2009).
52. Sahoo, P., Djieutedjeu, H. & Poudeu, P. F. P. Co₃O₄ nanostructures: the effect of synthesis conditions on particles size, magnetism and transport properties. *J. Mater. Chem. A* **1**, 15022 (2013).
53. Pfeil, T. L., Pourpoint, T. L. & Groven, L. J. Effects of crystallinity and morphology of solution combustion synthesized Co₃O₄ as a catalyst precursor in hydrolysis of sodium borohydride. *Int. J. Hydrogen Energy* **39**, 2149 (2014).
54. Morales, W., Cason, M., Aina, O., Tacconi, N. R. d. & Rajeshwar, K. Combustion synthesis and characterization of nanocrystalline WO₃. *J. Am. Ceram. Soc.* **130**, 6318 (2008).
55. Gupta, A., Ifeacho, P., Schulz, C. & Wiggers, H. *Proc. Combust. Inst.* **33**, 1883 (2011).
56. Pradhan, G. K., Martha, S. & Parida, K. M. Synthesis of multifunctional nanostructured zinc–iron mixed oxide photocatalyst by a simple solution-combustion technique. *ACS Appl. Mater. Interfaces* **4**, 707–713 (2012).
57. Reddy, B. M., Reddy, G. K., Rao, K. N., Ganesh, I. & Ferreira, J. M. F. Characterization and photocatalytic activity of TiO₂-M_xO_y (M_xO_y= SiO₂, Al₂O₃, and ZrO₂) mixed oxides synthesized by microwave-induced solution combustion technique. *J. Mater. Sci.* **44**, 4874 (2009).
58. Wang, D. & Astruc, D. Preparation and Characterization of Fe₂O₃/Al₂O₃ Using the Solution Combustion Approach for Chemical Looping Combustion. *Chem. Rev.* **114**, 6949–69585 (2014).
59. Zhang, J. S., Guo, Q. J., Liu, Y. Z. & Cheng, Y. Preparation and characterization of Fe₂O₃/Al₂O₃ using the solution combustion approach for chemical looping combustion. *Ind. Eng. Chem. Res.* **51**, 12773–12781 (2012).
60. Shang, N. *et al.* Suzuki–Miyaura reaction catalyzed by graphene oxide supported palladium nanoparticles. *Catal. Commun.* **40**, 111 (2013).
61. Kumar, A. *et al.* An investigation into the solar light-driven enhanced photocatalytic properties of a graphene oxide–SnO₂–TiO₂ ternary nanocomposite. *RSC Adv.* **6**, 32074–32088 (2016).
62. Tasca, J. E. *et al.* CuFe₂O₄ nanoparticles: A magnetically recoverable catalyst for selective deacetylation of carbohydrate derivatives. *Top. Catal.* **53**, 1087–1090 (2010).
63. Fu, Y. *et al.* Magnetically separable ZnFe₂O₄-graphene catalyst and its high photocatalytic performance under visible light irradiation. *Ind. Eng. Chem. Res.* **51**, 11700–11709 (2012).
64. Zhang, W. *et al.* One-step facile solvothermal synthesis of copper ferrite–graphene composite as a high-performance supercapacitor material. *ACS Appl. Mater. Interfaces* **7**, 2404–2414 (2015).
65. Yang, S. *et al.* One-pot synthesis of graphene-supported monodisperse Pd nanoparticles as catalyst for formic acid electro-oxidation. *Sci. Rep.* **4**, 4501 (2014).
66. Khalila, M. M. H., Ismaila, E. H., El-Baghdady, K. Z. & Mohameda, D. Green synthesis of silver nanoparticles using olive leaf extract and its antibacterial activity. *Arabian J. Chem.* **7**, 1131–1139 (2014).
67. Rout, L., Rengasamy, P., Ekka, B., Kumar, A. & Dash, P. Supported bimetallic AgSn nanoparticle as an efficient photocatalyst for degradation of methylene blue dye. *Nano* **10**, 1550059–1550072 (2015).
68. Tuinstra, F. & Koenig, J. L. Raman spectrum of graphite. *J. Chem. Phys.* **53**, 1126 (1970).
69. Marcano, D. C. *et al.* Improved synthesis of graphene oxide. *ACS Nano* **4**, 4806–4814 (2010).
70. Bilecka, I., Kubli, M., Amstad, E. & Niederberger, M. Simultaneous formation of ferrite nanocrystals and deposition of thin films via a microwave-assisted nonaqueous sol–gel process. *J. Sol-Gel Sci Technol* **57**, 313–322 (2011).
71. Matzen, S. *et al.* Epitaxial growth and ferrimagnetic behavior of MnFe₂O₄(111) ultrathin layers for room-temperature spin filtering. *Phys. Rev. B* **83**, 184402–184410 (2011).
72. Fu, Y. *et al.* Magnetically separable ZnFe₂O₄-graphene catalyst and its high photocatalytic performance under visible light irradiation. *Ind. Eng. Chem. Res.* **51**, 11700–11709 (2012).
73. Zhu, M., Meng, D., Wang, C. & Diao, G. Facile fabrication of hierarchically porous CuFe₂O₄ nanospheres with enhanced capacitance property. *ACS Appl. Mater. Interfaces* **5**, 6030–6037 (2013).
74. Liu, J. *et al.* A green approach to the synthesis of high-quality graphene oxide flakes via electrochemical exfoliation of pencil core. *RSC Adv.* **3**, 11745–11750 (2013).
75. Lalatonne, Y., Richardi, J. & Pileue, M. P. Van der Waals versus dipolar forces controlling mesoscopic organizations of magnetic nanocrystals. *Nat. Mater.* **3**, 121–125 (2004).
76. Bob, E., Hillringhaus, T., Nitsch, J. & Klusmann, M. Lewis acid-catalysed one pot synthesis of substituted xanthenes. *Org. Biomol. Chem.* **9**, 1744–1748 (2011).
77. Dreyer, D. R., Park, S., Bielawski, C. W. & Ruoff, R. S. The chemistry of graphene oxide. *Chem. Soc. Rev.* **39**, 228–240 (2010).
78. Wang, H. *et al.* Graphene oxide as a facile acid catalyst for the one-pot conversion of carbohydrates into 5-ethoxymethylfurfural. *Green Chem.* **15**, 2379–2383 (2013).
79. Dhakshinamoorthy, A., Alvaro, M., Concepcion, P., Fornes, V. & Garcia, H. Graphene oxide as an acid catalyst for the room temperature ring opening of epoxides. *Chem. Commun.* **48**, 5443–5445 (2012).
80. Kijenski, J. & Baiker, A. Acidic sites on catalyst surfaces and their determination. *Catal. Today* **5**, 1–120 (1989).
81. Ghorpade, S. P., Darshane, V. S. & Dixit, S. G. Liquid-phase Friedel–Crafts alkylation using CuCr_{2-x}Fe_xO₄ spinel catalysts. *Appl. Catal. B* **166**, 135–142 (1998).
82. Auroux, A. & Gervasini, A. Microcalorimetric study of the acidity and basicity of metal oxide surfaces. *J. Phys. Chem.* **94**, 6371–6379 (1990).
83. Tao, M. *et al.* Tailoring the synergistic bronsted-lewis acidic effects in heteropolyacid catalysts: Applied in esterification and transesterification reactions. *Sci. Rep.* **5** (2015).
84. Zhao, Y. *et al.* Graphene-Co₃O₄ nanocomposite as electrocatalyst with high performance for oxygen evolution reaction. *Sci. Rep.* **5**, 7629–7636 (2014).
85. Nur, H. *et al.* Synergistic role of Lewis and Brønsted acidities in Friedel–Crafts alkylation of resorcinol over gallium-zeolite beta. *Catal. Comm.* **12**, 822–825 (2011).
86. A.E.-Remaily, M. A. E. A. & A.-Dief, A. M. CuFe₂O₄ nanoparticles: an efficient heterogeneous magnetically separable catalyst for synthesis of some novel propynyl-1H-imidazoles derivatives. *Tetrahedron* **71**, 2579–2584 (2015).
87. Zhang, H., Lv, X., Li, Y., Wang, Y. & L. J. P25-Graphene Composite as a High Performance Photocatalyst. *ACS Nano* **4**, 380–386 (2010).
88. Perera, S. D. *et al.* Hydrothermal Synthesis of Graphene-TiO₂ Nanotube Composites with Enhanced Photocatalytic Activity. *ACS Catal.* **2**, 949–956 (2012).

89. Zubir, N. A., Yacou, C., Motuzas, J., Zhang, X. & Costa, J. C. D. Structural and functional investigation of graphene oxide-Fe₃O₄ nanocomposites for the heterogeneous Fenton-like reaction. *Sci. Rep.* **4**, 4594–4602 (2014).
90. Zhang, W. *et al.* One-step facile solvothermal synthesis of copper ferrite-graphene composite as a high-performance supercapacitor material. *ACS Appl. Mater. Interfaces* **7**, 2404–2414 (2015).
91. Oh, W.-D., Dong, Z., Hub, Z.-T. & Lim, T.-T. A novel quasi-cubic CuFe₂O₄-Fe₂O₃ catalyst prepared at low temperature for enhanced oxidation of bisphenol A via peroxymonosulfate activation. *J. Mater. Chem. A* **3**, 22208–22217 (2015).
92. Gohain, M. *et al.* Nano CuFe₂O₄: an efficient, magnetically separable catalyst for transesterification of b-ketoesters. *RSC Adv.* **5**, 18972–18976 (2015).
93. Esmailpour, M., Javidi, J., Dehghania, F. & Dodeji, F. N. Fe₃O₄@SiO₂-imid-PMAn magnetic porous nanospheres as recyclable catalysts for the one-pot synthesis of 14-aryl- or alkyl-14H-dibenzo[a, j]-xanthenes and 1,8-dioxooctahydroxanthene derivatives under various conditions. *New J. Chem.* **38**, 5453–5461 (2014).
94. Sajjadifar, S., Fadaeian, M., Bakhtiyari, M. & Rezayati, S. One-pot synthesis of xanthene derivatives using silica supported [2-(Sulfoxy)ethyl]sulfamic Acid as a novel and efficient catalyst under solvent-free condition. *Chem. Sci. Trans.* **3**, 107 (2014).
95. Eshghi, H., Bakavoli, M. & Moradi, H. Fe(HSO₄)₃: An efficient, heterogeneous and reusable catalyst for the synthesis of 14-aryl- or alkyl-14H-dibenzo[a, j]xanthenes. *Chin. Chem. Lett.* **19**, 1423–1426 (2008).
96. Mondal, J., Nandi, M., Modak, A. & Bhaumik, A. Functionalized mesoporous materials as efficient organocatalysts for the syntheses of xanthenes. *J. Mol. Catal. A: Chem.* **363–364**, 254 (2012).
97. Verma, K. G., Raghuvanshi, K., Verma, R. K., Dwivedi, P. & Singh, M. S. An efficient one-pot solvent-free synthesis and photophysical properties of 9-aryl/alkyl-octahydroxanthene-1, 8-diones. *Tetrahedron Lett.* **67**, 3698 (2011).
98. Rama, V., Kanagaraj, K. & Pitchumani, K. A multicomponent, solvent-free, one-pot synthesis of benzoxanthenones catalyzed by HY zeolite: their anti-microbial and cell imaging studies. *Tetrahedron Lett.* **53**, 1018 (2012).
99. Nagarapu, L., Kantevari, S., Mahankhali, V. C. & Apuri, S. Potassium dodecatungstocobaltate trihydrate (K₅CoW₁₂O₄₀·3H₂O): A mild and efficient reusable catalyst for the synthesis of aryl-14H-dibenzo[a, j]xanthenes under conventional heating and microwave irradiation. *Catal. Commun.* **8**, 1173–1177 (2007).
100. Park, S. J. *et al.* Aqueous suspension and characterization of chemically modified graphene sheets. *Chem. Mater.* **20**, 6592–6594 (2008).
101. Kudin, K. N. *et al.* Raman spectra of graphite oxide and functionalized graphene sheets. *Nano Lett.* **8**, 36–41 (2008).
102. Xu, Y., Sheng, K., Li, C. & Shi, G. Self-assembled graphene hydrogel via a one-step hydrothermal process. *ACS Nano* **4**, 4324–4330 (2010).

Acknowledgements

The authors are thankful to Department of Science & Technology (DST), Govt. of India, for funding. XPS facility at IIT Delhi is partially funded by FIST grant of DST, India.

Author Contributions

P.D. designed the study and reviewed the manuscript. A.K. performed experiments, analysed data, and wrote the manuscript. L.R. help in analysing data, L.S.K.A. reviewed the manuscript and R.S.D. performed XPS measurements and analysed data.

Additional Information

Supplementary information accompanies this paper at <http://www.nature.com/srep>

Competing financial interests: The authors declare no competing financial interests.

How to cite this article: Kumar, A. *et al.* Greener Route for Synthesis of aryl and alkyl-14H-dibenzo [a, j] xanthenes using Graphene Oxide-Copper Ferrite Nanocomposite as a Recyclable Heterogeneous Catalyst. *Sci. Rep.* **7**, 42975; doi: 10.1038/srep42975 (2017).

Publisher's note: Springer Nature remains neutral with regard to jurisdictional claims in published maps and institutional affiliations.



This work is licensed under a Creative Commons Attribution 4.0 International License. The images or other third party material in this article are included in the article's Creative Commons license, unless indicated otherwise in the credit line; if the material is not included under the Creative Commons license, users will need to obtain permission from the license holder to reproduce the material. To view a copy of this license, visit <http://creativecommons.org/licenses/by/4.0/>

© The Author(s) 2017